MOLECULAR PHYSICS, 1995, VOL. 84, NO. 5, 995–1020

RF-driven and proton-driven NMR polarization transfer for investigating local order

An application to solid polymers

By P. ROBYR†, M. TOMASELLI‡, J. STRAKA†§, C. GROB-PISANO‡‖, U. W. SUTER‡, B. H. MEIER¶ and R. R. ERNST†

† Laboratorium für Physikalische Chemie and ‡ Institut für Polymere, Eidgenössische Technische Hochschule, CH-8092 Zürich, Switzerland

¶ NSR-Center for Molecular Structure, Design and Synthesis, Laboratory of Physical Chemistry, University of Nijmegen, Toernooiveld, 6525 ED Nijmegen, The Netherlands

(*Received 1 December 1994; accepted 15 December 1994*)

A comparative study of proton-driven and radio-frequency-driven polarization-transfer processes in NMR of rare spins is presented in view of investigating order in partially disordered solids. The results exemplify the complementary use of the two techniques: proton-driven polarization transfer for recording quasi-equilibrium spectra that characterize long-range order, and radio-frequency-driven transfer for the measurement of geometrical rate factors from which information about local order is obtained. Procedures are described for the evaluation of polarization-transfer data. The techniques are applied to the study of order in amorphous samples of atactic polystyrene and syndiotactic poly(methyl methacrylate). In polystyrene, orientational correlation among the phenyl groups is found within a range of 5 Å. In poly(methyl methacrylate), local order is below the detection limit.

1. Introduction

The internuclear magnetic dipolar interaction, that can be observed by solid-state nuclear magnetic resonance (NMR), has become a rich source of structural information [1, 2]. For isolated pairs of spins, the dipolar interaction causes a line splitting that can easily be measured and interpreted. For samples with many coupled spins, the dipolar interaction can be utilized for a spatial transfer of polarization, often called spin diffusion [3, 4]. The transfer process yields useful information on the local structure in crystalline and amorphous materials [5–12]. Since the dipolar coupling strength rapidly decreases with increasing internuclear distance, NMR well complements X-ray and neutron diffraction for studying local order in amorphous solids where the lack of translational symmetry renders the use of scattering techniques difficult [13].

Two-dimensional (2D) polarization-transfer NMR spectroscopy [14] was used for measuring the relative orientation of chemical shielding anisotropy (CSA) tensors in powder samples by Edzes and Bernards [15] and by Henrichs and Linder [16]. More recently, Tycko and Dabbagh [8–10] and Robyr *et al.* [11, 12] obtained

§ Present address: Institute of Macromolecular Chemistry, Academy of Science of the Czech Republic, 162 06 Prague 6, Czech Republic.

‖ Present address: Du Pont de Nemours & Co., Inc., Central Research and Development, Wilmington DE 19898, USA.

0026-8976/95 $10.00

structural information on crystalline and glassy materials from 2D polarization-transfer correlation maps.

Two-dimensional polarization-transfer spectra can be recorded either as quasi-equilibrium spectra with an extended polarization-transfer period or in the initial rate regime using a short polarization-transfer period. Quasi-equilibrium spectra provide little distance information but allow one to correlate the relative orientation of CSA tensors in polycrystalline samples [8, 11] and in amorphous substances [9, 10]. They also provide information on heterogeneous systems with domain sizes exceeding 100 Å [17].

The quantitative evaluation of distances within the unit cell of crystalline phases or of short-range order in amorphous materials requires measuring polarization-transfer rate constants between specific sites. According to a second-order perturbation treatment of spin diffusion [3] the polarization-transfer rate constant W_{ij} between the spins i and j is given by

$$W_{ij} = \frac{\pi}{2} b_{\mathrm{eff},ij}^2 F_{ij}(0) = \frac{\pi}{2} s_{ij}^2 b_{ij}^2 F_{ij}(0), \tag{1}$$

where $b_{\mathrm{eff},ij}$ denotes the effective dipolar coupling frequency containing the dipolar scaling factor s_{ij} that depends on the Hamiltonian active in the polarization-transfer period of the experiment. The dipolar coupling frequency

$$b_{ij} = -\frac{\mu_0}{4\pi} \frac{\gamma_S^2 \hbar}{r_{ij}^3} \frac{1}{2} (3 \cos^2 \theta_{ij} - 1) \tag{2}$$

depends purely on geometrical factors, namely the internuclear distance r_{ij} and the angle θ_{ij} between the static magnetic field and the internuclear vector. For laboratory-frame polarization transfer, the scaling factor s_{ij} is 1 for all i and j, while for on-resonance rotating-frame experiments $s_{ij} = -\frac{1}{2}$. The term $F_{ij}(0)$ is the intensity of the normalized zero-quantum (ZQ) transition spectrum $F_{ij}(\omega)$ (flip–flop transition of two spins) at zero frequency [3, 18]. The perturbation approach which leads to equation (1) requires that the effective dipolar coupling $b_{\mathrm{eff},ij}$ is smaller than the homogeneous line-width of the zero-quantum spectrum. The proportionality of W_{ij} to $F_{ij}(0)$ is the major difficulty in interpreting the polarization-transfer rate constants in terms of internuclear distances. The shape of $F_{ij}(\omega)$ depends on the dipolar interaction of spins i and j to extraneous spins, and its frequency shift is given by the resonance frequency difference of the two spins as visualized in figure 1. Procedures to separate the two factors b_{ij}^2 and $F_{ij}(0)$ will be discussed in this paper.

Two experimental schemes for the measurement of polarization transfer among

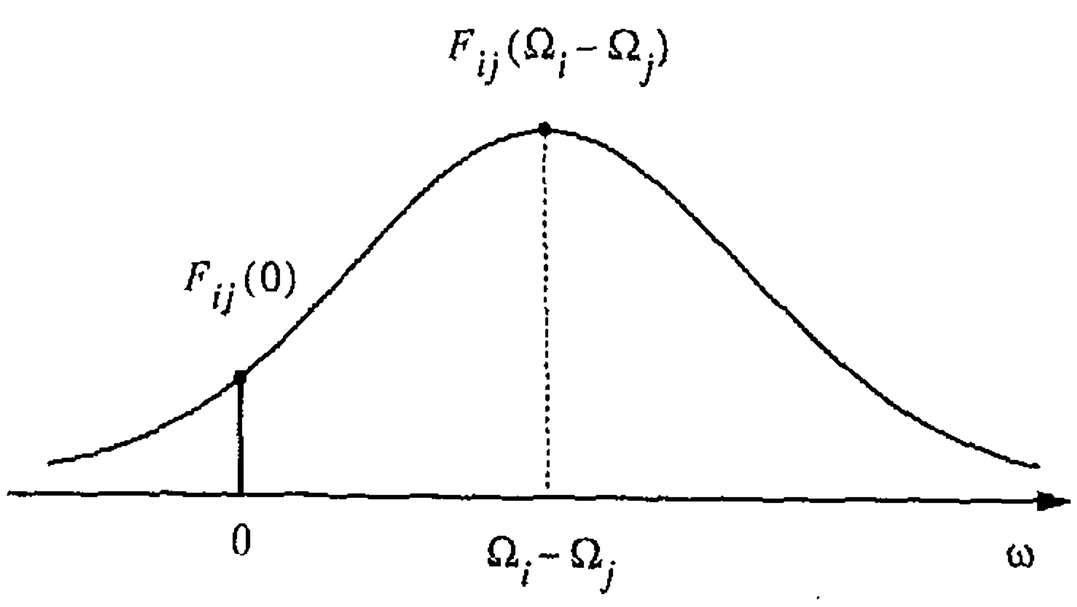

Figure 1. Zero-quantum spectrum $F_{ij}(\omega)$ of the flip–flop transition of two spins S_i and S_j with the rotating frame frequencies Ω_i and Ω_j.

low-γ S spins (e.g. ^{13}C or ^{15}N) in the presence of abundant high-γ spins (usually ^{1}H) will be analysed and applied. In the proton-driven polarization-transfer experiment of figure 2 (*a*), polarization transfer among the S spins occurs in the presence of the I–S and I–I dipolar interactions that govern the line shape of the ZQ spectrum $F_{ij}(\omega)$. The spread of S-spin chemical shieldings might well exceed the width of the ZQ spectrum and introduce a strong dependence of the polarization-transfer rate constant on the spectral separation of the spins. In addition, the orientation-dependent heteronuclear couplings can cause a variation of the ZQ spectrum with the orientation of the sample. Such a situation is common for carbons with directly bonded protons. Both dependences propagate to the observed rate constants and complicate their interpretation in terms of spatial information.

During the mixing period of radio-frequency (RF)-driven polarization-transfer experiments (figure 2 (*b*)), the S-spin magnetization is spin-locked in the transversal plane [19] and thus decoupled from the I spins. The width of the ZQ spectrum is narrowed and its peak intensity increased compared to the proton-driven case since it is determined solely by the homonuclear dipolar interactions among the S spins. At the same time, the apparent resonance frequency difference of the spins S_i and S_j is reduced, moving the ZQ flip–flop transition close to zero frequency. If the frequency of the flip–flop transitions is smaller than the zero-quantum line-width, a strongly enhanced polarization-transfer rate constant is obtained that becomes, under ideal conditions, virtually independent on frequency offsets.

In this paper, we analyse the two polarization-transfer experiments for their application to semicrystalline and amorphous materials. We provide an appropriate data analysis procedure for the proton-driven transfer that takes into account the shape of the ZQ spectrum. The polarization-transfer experiments are applied to atactic and isotactic polystyrene (a-PS and i-PS, respectively) and to syndiotactic poly(methyl methacrylate) (s-PMMA). For amorphous atactic polystyrene information about the local ordering of the phenyl rings is obtained.

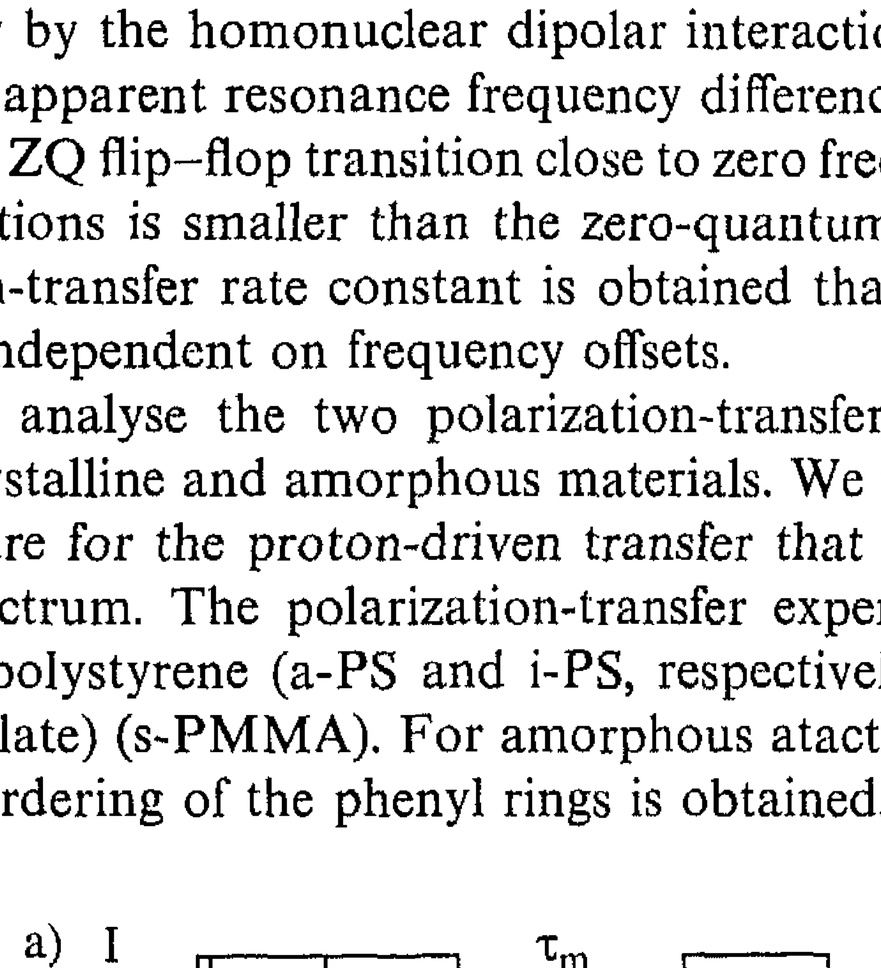

Figure 2. Experimental schemes for (*a*) proton-driven and (*b*) RF-driven polarization transfer. During the mixing time, S-spin magnetization is stored along the z-axis in the proton-driven experiment, whereas it is spin-locked along the x-axis of the rotating frame in the RF-driven polarization-transfer experiment. Homonuclear decoupling of the I spins is applied during the spin-locking period.

We focus in the following on static samples. The necessary chemical site resolution is obtained by isotopic enrichment. However, similar experiments can be extended to rotating samples by using zero-angle-spinning (ZAS) [20]. The 2D polarization-transfer pulse scheme performed at zero angle is flanked by one or two additional time periods during which the sample rotates at the magic angle. In the resulting three-dimensional (3D) or four-dimensional (4D) spectra, the 2D powder exchange patterns are resolved in the first and/or the fourth dimension according to the isotropic chemical shifts of the S spins.

2. Polarization-transfer rate constants and geometrical rate factors between two spin groups

Equation (1) gives the polarization-transfer rate constant for two isolated spins S_i and S_j in the presence of an external broadening mechanism. The situation in a typical static solid sample, either with natural abundance or isotopically enriched S spins, is different: the cross-peak intensity at the frequency coordinates $\omega_1 = \Omega_A$ and $\omega_2 = \Omega_B$ originates from the transfer between many spins with resonance frequencies in the small resolution intervals $\Omega_A \pm \delta/2$ and $\Omega_B \pm \delta/2$. This requires a reinterpretation of the polarization-transfer rate constant and complicates the separation of the geometrical and spectral parts in equation (1).

We consider at first N coupled non-equivalent spins S_k with the polarization $p_k(t)$ and whose resonance lines do not overlap. The polarization transfer is determined by the matrix W. Its elements W_{ij} are given by equation (1) and $W_{jj} = -\sum_{i \neq j} W_{ij}$. Neglecting relaxation effects, the polarization vector $\mathbf{p} = (p_1, \ldots, p_N)$ evolves according to the master equation

$$\frac{\mathrm{d}}{\mathrm{d}t}\,\mathbf{p} = W\mathbf{p}. \tag{3}$$

Assuming an initial state with a single spin polarized, $p_k(0) = p_j(0)\delta_{kj}$, the solution for $p_i(\tau_m)$ is

$$p_i(\tau_m) = [\exp(W\tau_m)]_{ij}\, p_j(0). \tag{4}$$

Since the total polarization is preserved and assuming that all spins communicate, the final state is an equal distribution among all spins:

$$\lim_{\tau_m \to \infty} p_i(\tau_m) = p_i^{\mathrm{eq}} = \frac{p_j(0)}{N}. \tag{5}$$

Thus,

$$p_i(\tau_m) = [\exp(W\tau_m)]_{ij} N p_i^{\mathrm{eq}}. \tag{6}$$

The cross-peak intensity in the 2D polarization-transfer spectrum $I_{ij}(\tau_m)$ is proportional to $p_i(\tau_m)$ and one obtains

$$I_{ij}(\tau_m) = [\exp(W\tau_m)]_{ij} N I_{ij}^{\mathrm{eq}}. \tag{7}$$

For a sufficiently short mixing time τ_m, the initial rate approximation holds and the cross-peak intensity $I_{ij}(\tau_m)$ is [14]

$$I_{ij}(\tau_m) = W_{ij}\tau_m N I_{ij}^{\mathrm{eq}}. \tag{8}$$

We assume now that K groups of n_Q lines in the frequency interval $\Omega_Q \pm \delta/2$ overlap.

Generally, only their sum polarizations P_Q can be detected,

$$P_Q = \sum_{i \in Q} p_i. \tag{9}$$

The sum runs over all spins i that have their resonance frequency in the interval $\Omega_Q \pm \delta/2$. To follow the time evolution of the sum polarizations, it is convenient to perform a basis transformation of the polarization vector:

$$\mathbf{L}\begin{bmatrix} p_1 \\ \vdots \\ p_i \\ \vdots \\ p_N \end{bmatrix} = \begin{bmatrix} P_1 \\ \vdots \\ P_A \\ \vdots \\ P_K \\ \hline D_1 \\ \vdots \\ D_{N-K} \end{bmatrix} = \begin{bmatrix} \mathbf{S} \\ \hline \mathbf{D} \end{bmatrix}. \tag{10}$$

The first K components represent the sum polarizations of the K groups of isochronous spins and are collected in the vector **S**. The remaining $N-K$ linear combinations D_Q are orthogonal to the sums and form the vector **D**. The master equation in the new basis reads

$$\frac{\mathrm{d}}{\mathrm{d}t}\begin{bmatrix} \mathbf{S} \\ \mathbf{D} \end{bmatrix} = \mathbf{W}^L \begin{bmatrix} \mathbf{S} \\ \mathbf{D} \end{bmatrix} = \begin{bmatrix} \mathbf{W}^{SS} & \mathbf{W}^{SD} \\ \mathbf{W}^{DS} & \mathbf{W}^{DD} \end{bmatrix} \begin{bmatrix} \mathbf{S} \\ \mathbf{D} \end{bmatrix} \tag{11}$$

where the kinetic matrix $\mathbf{W}^L$ is given by $\mathbf{W}^L = \mathbf{L}\mathbf{W}\mathbf{L}^{-1}$. The conservation of polarization requires that the sum over the column vectors of $\mathbf{W}^{SS}$ vanish. Except for special cases, $\mathbf{W}^L$ is not block diagonal and the full matrix has to be considered. Nevertheless, if differential relaxation of the n_Q spins during the preparation and the evolution period of the 2D experiments in figure 2 can be neglected, the part **D** of the polarization vector starts the mixing process with all its elements equal to zero. Thus, the initial time evolution of the observable sum polarizations in **S** is exclusively determined by the upper left block $\mathbf{W}^{SS}$. We consider the transfer from the spin group B at Ω_B to the spin group A at Ω_A. In analogy to equation (8), we obtain

$$I_{AB}(\tau_m) = W^{SS}_{AB}\tau_m \frac{N}{n_A} I^{\mathrm{eq}}_{AB}, \tag{12}$$

where I^{eq}_{AB} is the quasi-equilibrium intensity of the n_A spins of group A after a uniform distribution of the initial B-spin intensity $I^{\mathrm{eq}}_{AB}(N/n_A)$ among the N spins of the sample. The rate constant W^{SS}_{AB} is the average sum of all rate constants leading from one spin of group B to all spins of group A:

$$W^{SS}_{AB} = \frac{1}{n_B} \sum_{i \in A} \sum_{j \in B} W_{ij}, \qquad \text{for } A \neq B. \tag{13}$$

From equation (12), the relative cross-peak intensity in the initial rate regime is

$$\frac{I_{AB}(\tau_m)}{I_{AB}^{eq}} = \frac{N}{n_A} W_{AB}^{SS} \tau_m = R_{AB} \tau_m. \tag{14}$$

The corresponding cross-peak grows with the rate constant R_{AB} towards its equilibrium intensity. R_{AB} is preferred to W_{AB}^{SS} because of the symmetry, $R_{AB} = R_{BA}$. It can easily be obtained from 2D experiments via equation (14). Later it will also become apparent that the variations of R_{AB} directly reveal local order when all intensities of the ZQ spectra $F_{ij}(0)$ appearing in the rate constants W_{ij} are equal. Combining equations (13), (14), and (1) leads to

$$R_{AB} = \frac{N}{n_A n_B} \sum_{i \in A} \sum_{j \in B} W_{ij} = \frac{N}{n_A n_B} \frac{\pi}{2} \sum_{i \in A} \sum_{j \in B} s_{ij}^2 b_{ij}^2 F_{ij}(0). \tag{15}$$

Because s_{ij}^2 depends only on the resonance frequencies of the isochromates A and B, it can be replaced by s_{AB}^2 and moved in front of the summation. For a general case, the interpretation of a measured value for R_{AB} in terms of spatial order, described by b_{ij}^2, is difficult. Each dipolar contribution b_{ij}^2 in the double sum of equation (15) must be weighted with a line-shape contribution $F_{ij}(0)$ and the sum must be evaluated explicitly. If, however, all involved zero quantum transitions that contribute to the isochromates A and B have the same intensities at zero frequency, i.e.

$$F_{ij}(0) = F_{AB}(0), \qquad \text{for all } i \text{ and } j \text{ with } \Omega_i = \Omega_A \text{ and } \Omega_j = \Omega_B, \tag{16}$$

it is possible to average separately the dipolar frequency contributions b_{ij}^2 and to rewrite equation (15), in analogy to equation (1), in the form

$$R_{AB}(\Omega_A, \Omega_B) = \frac{\pi}{2} s_{AB}^2 g_{AB} F_{AB}(0). \tag{17}$$

g_{AB} is the geometrical rate factor between the spin groups A and B:

$$g_{AB} = \frac{N}{n_A n_B} \sum_{i \in A} \sum_{j \in B} b_{ij}^2. \tag{18}$$

It contains the structural information carried by the rate constant R_{AB}. If order is present, the orientation of the CSA tensors is correlated with the mean square coupling frequency that appears in equation (18) and the variations of the geometrical rate factor g_{AB} reveal local order. At first, the multiplication with the total number of spins N might seem inappropriate. However, if one considers the summation over macroscopic sample volumes where the number of summed terms is very large, but only very few of them contribute significantly to g_{AB}, the role of N becomes obvious as it renders g_{AB} independent of the size of the sample. The only parameter that still needs to be determined is the spectral rate factor $F_{AB}(0)$.

Except for selected spin pairs in single crystal samples [21] a direct experimental determination of $F_{ij}(0)$ is difficult. As an approximation $F_{ij}(0)$ can be estimated from the convolution of the single-quantum (1Q) spectra $f_i(\omega)$ and $f_i(\omega)$ of the spins i and j [3, 22, 23]:

$$F_{ij}(0) = [f_i(\omega) * f_j(-\omega)](0). \tag{19}$$

This approximation assumes that the dipolar fields at sites i and j owing to 'extraneous spins' are not correlated [24] and that the 1Q lineshapes are homogeneous

[18]. In addition, it disregards the line-shape contribution of the dipolar coupling between the spins i and j. If

$$f_k(\omega) = f_l(\omega), \qquad \text{for all spins } k \text{ and } l \text{ in each isochromate,} \tag{20}$$

a condition that has to be verified on a case by case basis, $f_i(\omega)$ and $f_j(\omega)$ can be replaced by the sum line-shapes $f_A(\omega)$ and $f_B(\omega)$, respectively, and

$$F_{AB}(0) = [f_A(\omega) * f_B(-\omega)](0). \tag{21}$$

If the zero-quantum line-shapes of all spin pairs that resonate at frequencies (Ω_A, Ω_B) are the same, equations (17), (18), and (21) form the basis for studying local order with polarization-transfer techniques.

If the separation of the geometrical and the spectral contributions as in equation (17) is not feasible because of variations of the 1Q spectra within a given isochromate, the rate constants R_{AB} must be evaluated according to equation (15) as a complicated average over products of coupling frequencies and zero-quantum line intensities. The interpretation of experimental data then requires a molecular model that includes the interactions which control the variations of the ZQ line-shape as well.

3. The two polarization-transfer experiments

3.1. *Proton-driven polarization transfer*

The basic proton-driven polarization-transfer experiment is shown in figure 2 (*a*). During the preparation period, *S*-spin coherence is generated by Hartmann–Hahn cross polarization. It freely precesses during the evolution period in the presence of *I*-spin decoupling. The mixing period is preceded by a $\pi/2$ *S*-spin pulse that converts the coherence into polarization. *S* spins are allowed to exchange their polarization during the mixing period under a Hamiltonian containing the chemical shielding interactions, and the homonuclear and heteronuclear dipolar interactions of the *S* and *I* spins. A second $\pi/2$ *S*-spin pulse terminates the mixing process and precedes detection, proceeding again under *I*-spin decoupling.

The line-width of the ZQ spectrum $F_{ij}(\omega)$, that is required to evaluate geometrical rate factors from experimental polarization-transfer rate constants through equation (17), is given by the *I–S* and the *I–I* dipolar interactions, while its centre frequency $\Omega_i - \Omega_j$ is equal to the chemical shielding difference of the two spins S_i and S_j, as shown in figure 1. Several drawbacks have their roots in these dependencies of the ZQ spectrum when polarization-transfer measurements are used for structural studies. (i) The position of the ZQ spectrum centre at $\Omega_i - \Omega_j$ introduces a strong frequency dependence of the polarization-transfer rate constant, especially in high magnetic fields where the range of chemical shielding can significantly exceed the dipolar line-width of the ZQ spectrum. (ii) For *S* spins with directly bonded *I* spins, the dominant heteronuclear dipolar interactions cause a strong orientational dependence of the dipolar line-width of the ZQ spectrum. Both effects lead to variations of the rate constants throughout the 2D spectrum. They are difficult to correct and impede the interpretation of the polarization transfer data in terms of geometrical rate factors and structural information. (iii) The strong heteronuclear dipolar broadening of the zero-quantum line causes low ZQ intensities and thus low transfer rate constants.

For methyl groups, where the ^{13}C chemical shielding tensor is nearly axially

symmetric and coaxial with the averaged heteronuclear dipolar interaction or for ^{13}C without directly attached protons, all 1Q spectral contributions $f_i(\omega)$, for a given resonance frequency Ω_i, are nearly identical. Then, the geometrical rate factor can be extracted from the rate constants R_{AB} through equation (17) using $F_{AB}(0)$ as evaluated from equation (21) based on experimental 1Q spectra. However, in case of strong variations of $F_{AB}(0)$ as a function of (Ω_A, Ω_B) this procedure may introduce large errors in g_{AB}.

3.2. *Radio-frequency-driven polarization transfer*

The RF-driven polarization-transfer experiment of figure 2 (*b*) differs from the proton-driven transfer by the presence of a strong spin-locking RF field on the *S* channel during the mixing period. This removes the three disadvantages mentioned for the proton-driven transfer. (i) In the case of continuous wave irradiation, the resonance-frequency differences are scaled by the RF-field of amplitude ω_1 according to

$$\Omega_i^s - \Omega_j^s = (\Omega_i^2 + \omega_1^2)^{1/2} - (\Omega_j^2 + \omega_1^2)^{1/2} \approx (\Omega_i - \Omega_j)\,\frac{\Omega_i + \Omega_j}{2\omega_1} \qquad (22)$$

where the approximation is valid for $\omega_1 \gg \Omega_i, \Omega_j$. Under these conditions the dipolar scaling factor is $s_{ij} = -1/2$. (ii) Spin locking leads to heteronuclear decoupling and removes the effects of the *I*–*S* interaction. The dipolar line-width is determined exclusively by the *S*–*S* dipolar interactions. In natural abundance and for single-site *S*-spin labelled samples where many rather remote *S* spins contribute to the width of the ZQ spectrum of a spin pair, the homonuclear dipolar width has little orientation dependence. (iii) The much reduced line-width of the ZQ spectrum causes high peak intensities. Due to the scaled chemical shielding difference, the ZQ spectrum $F_{ij}(\omega)$ is sampled close to its maximum. This effect more than balances the smaller dipolar scaling factor of the RF-driven experiment so that the polarization-transfer rate constants are considerably larger than in the proton-driven experiment. Combined with (ii), it also leads to a uniform intensity of the ZQ spectrum $F_{ij}(0)$. Then, the spectral rate factors $F_{AB}(0)$ in equation (17) are almost equal not only for spin pairs with the same resonance frequencies but over the whole 2D spectrum:

$$F_{AB}(0) = F(0). \qquad (23)$$

Under this condition, the rate constants R_{AB} of equation (17) are directly proportional to g_{AB} and any variation of R_{AB} plotted as a function of (Ω_A, Ω_B) directly reveals local order.

The scaling of the chemical shielding frequencies described by equation (22) can be much improved by using multiple-pulse sequences for spin-locking [18, 19, 25]. In the following, we will focus on the WALTZ17 sequence with which the experimental results in this paper were obtained. Discussion and comparison of several pulse sequences can be found in [18] and [25]. The WALTZ17 sequence [26] is defined by $(\bar{3}4\bar{2}3\bar{1}2\bar{4}2\bar{3}\ 3\bar{4}2\bar{3}1\bar{2}4\bar{2}3\ 3\bar{4}2\bar{3}1\bar{2}4\bar{2}3\ \bar{3}4\bar{2}3\bar{1}2\bar{4}2\bar{3}\ \alpha)_n$ where 1 stands for a $\pi/2$ pulse, 2 for a π pulse, 3 for a $3\pi/2$ pulse, and 4 for a 2π pulse. The bar indicates a π-phase shift, and α is the flip-angle of the '17th' pulse.

We consider a system of two dipolar coupled *S* spins under the influence of a

WALTZ17 sequence. The average homonuclear Hamiltonian up to first order is given by [18]

$$\bar{H}_{ij} = \bar{H}_{ij}^{(0)} + \bar{H}_{ij}^{(1)} + \bar{\omega}(S_{ix} + S_{jx})$$
$$= s_{ij} b_{ij}(3S_{ix}S_{jx} - \mathbf{S}_i \cdot \mathbf{S}_j) + \bar{\omega}\left(\frac{\Omega_i^2}{2\omega_1} S_{ix} + \frac{\Omega_j^2}{2\omega_1} S_{jx}\right) + \bar{\omega}(S_{ix} + S_{jx}). \qquad (24)$$

$\bar{H}_{ij}^{(k)}$ denotes the secular average Hamiltonian of kth order in the toggling frame. ω_1 is the amplitude of the spin lock field and $\bar{\omega} = (\alpha/(48\pi + \alpha))\omega_1$ the average spin-lock field strength. The dipolar scaling factor is $s_{ij} = -\frac{1}{2}$.

The 17th pulse is required to provide an effective spin-locking field (last term in equation (24)) [18, 19]. In its absence higher-order terms in the average Hamiltonian cause a rapid decay of the polarization. On the other hand, the 17th pulse leads to a residual chemical shielding term (second term in equation (24)). For $\alpha = \pi/2$, the chemical shielding Ω_i is scaled by a factor $\Omega_i/(194\omega_1)$. The duration of the spin-lock pulse must be long enough to provide a sufficiently strong effective spin-locking field that inhibits the decay of the spin polarization but remains short enough to allow for an efficient reduction of the chemical shielding differences.

To evaluate the off-resonance performance of the WALTZ17 sequence beyond the limits of first-order average Hamiltonian theory, the effective Hamiltonian was calculated numerically. The time-dependent Hamiltonian introduces a sequence of unitary transformations. Their effect during the cycle time τ_c can be represented by an effective Hamiltonian $\bar{H}_{\text{eff}}$:

$$U(\tau_c) = \prod_k \exp(-iH_k\tau_k) = \exp(-i\bar{H}_{\text{eff}}\tau_c), \qquad \tau_c = \sum_k \tau_k. \qquad (25)$$

$\bar{H}_{\text{eff}}$ can be computed from $U(\tau_c)$ by the logarithmic relation

$$\bar{H}_{\text{eff}} = \frac{-i}{\tau_c} \ln[U(\tau_c)]. \qquad (26)$$

The numerical solution of equation (26) is not unique [27] because of the periodic nature of the exponential function. This leads to difficulties when the parametric dependence of $\bar{H}_{\text{eff}}$ is investigated or plotted. To obtain a unique solution, the equation is transformed into an interaction frame rotating with the average RF field strength $\bar{\omega}$, where the average effect of the sequence is neutralized. The time-dependent interaction-frame Hamiltonian is then

$$H^{\alpha}(t) = \exp(-i\bar{\omega}F_x t)[H(t) - \bar{\omega}_{\text{rf}}F_x]\exp(i\bar{\omega}F_x t), \qquad (27)$$

with the total spin operator $F_x = \sum_i S_{ix}$. For computing the corresponding propagator $U^{\alpha}(\tau_c)$, each time-dependent pulse is divided into short increments, 100 increments for the numerical calculations presented below, and an expression of the type of equation (25) is evaluated.

The scaling of the chemical shielding difference for WALTZ17 with a spin-lock pulse $\alpha = \pi/2$ at a field strength of 100 kHz is shown in figure 3 (*a*). The differences are scaled within an offset range of 6 kHz to less than 6 Hz. The scaling of the dipolar interactions s_{ij} is plotted in figure 3 (*b*). As expected, a scaling factor of $-1/2$ is found on-resonance. Within an offset of 6 kHz, $s_{ij}(\Omega_i, \Omega_j)$ deviates by less than 0·02 from $-0{\cdot}5$. The scaling of the homonuclear dipolar Hamiltonian depends almost exclusively on the sum of the offsets. The scaling factor hardly varies along a line perpendicular to the diagonal.

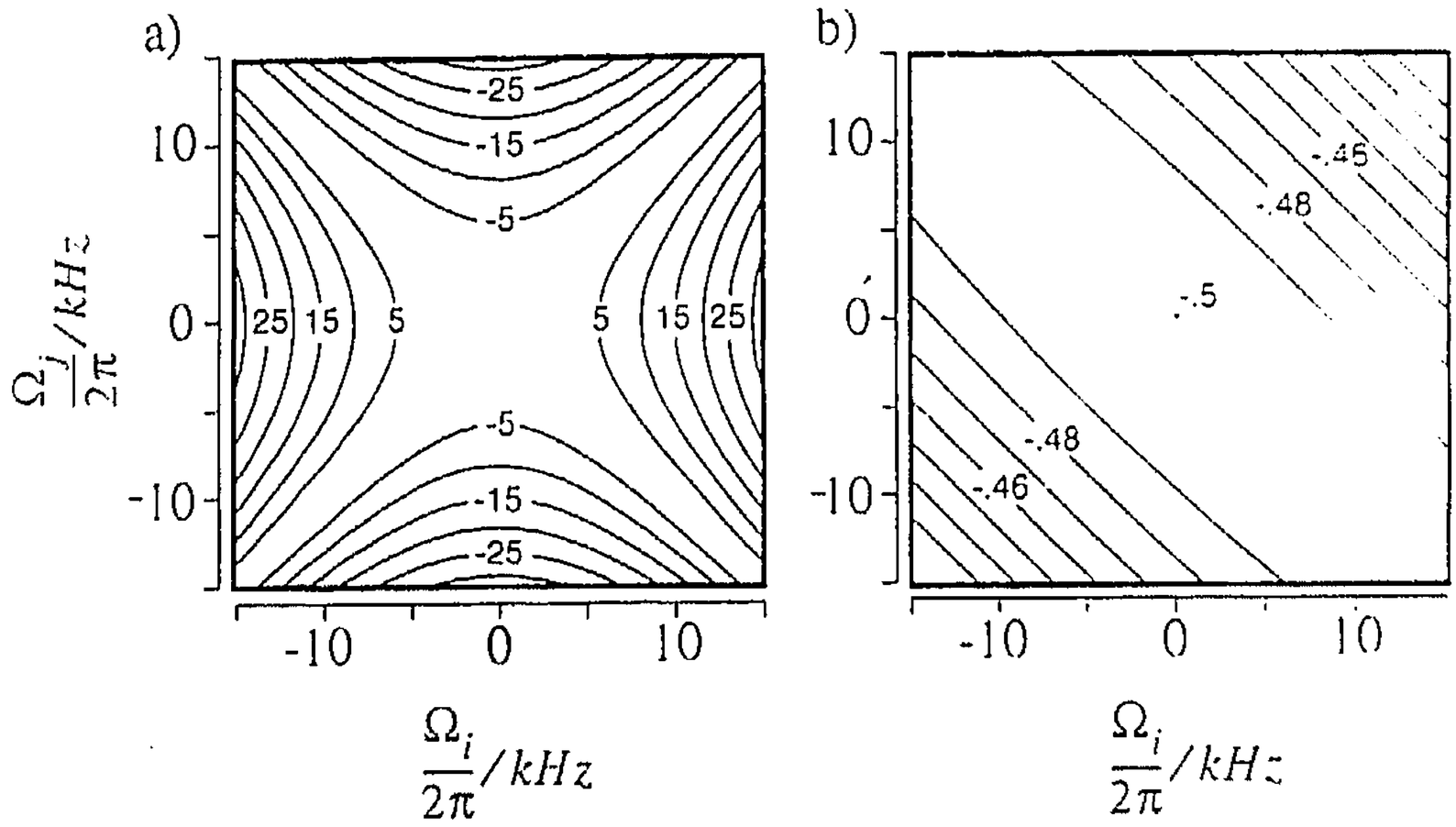

Figure 3. Scaling of the interactions in a 2D rotating frame polarization-transfer experiment under WALTZ17 irradiation with a spin locking pulse $\alpha = \pi/2$. (*a*) Scaled chemical shielding difference and (*b*) scaling factor s_{ij} of the dipolar coupling constant as functions of the two rotating frame resonance frequencies Ω_i and Ω_j. The assumed RF-field strength is 100 kHz and the dipolar coupling constant 170 Hz. 50 × 50 data points were computed. At $\Omega_i = \Omega_j = 0$, the dipolar scaling is $-0{\cdot}5$.

A continuous wave spin-locking of the S spins provides significantly better decoupling from the I spins than a WALTZ17 sequence that suffers from the weak effective RF field with the average amplitude $\omega_1\alpha/(48\pi + \alpha)$. It cannot sufficiently suppress the effects of the dipolar fluctuations within the I-spin bath, as explained in [18]. This leads to a rapid decay of the spin-locked S-spin polarization in particular for rigid solids with strong I–I interactions.

It thus desirable to eliminate the effects of the heteronuclear I–S interactions by additional I-spin decoupling. From the work of Haeberlen [28] and others it is known that heteronuclear continuous wave (CW) decoupling in the presence of a homonuclear multipulse sequence works only for discrete amplitude values. In [29] it was found experimentally that WALTZ sequences can be applied simultaneously with windowless BLEW sequences [30] to improve the heteronuclear decoupling efficiency of WALTZ. By combining the WALTZ17 sequence with a BLEW12 irradiation to the protons at $\omega_1^{1H} = \omega_1^{13C} = 100$ kHz, we were able to lengthen $T_{1\rho}^{13C}$ by a factor of two to five depending on the strength of the heteronuclear dipolar interactions. Eight BLEW12 cycles fit exactly in the duration of a WALTZ16 cycle. No irradiation to the protons is applied during the 17th pulse. This combination is successful when the carbons have no attached protons. In the presence of directly bonded protons, a partial decay of the polarization still occurs in the first few milliseconds of the spin-locking experiment.

The imperfect performance of the combination WALTZ17/BLEW12 arises probably from the misfit caused by the 17th pulse. To eliminate it, the sequence was changed to WALTZ16, however with the $+x$ pulse amplitude 2% larger than for the $-x$ pulses. This modified sequence, denoted by WALTZ16E, where the final E stands for 'effective field', has the same average spin-lock field strength and performs for polarization transfer as well as the WALTZ17 with a $\pi/2$ 17th-pulse. However, it has better spin-locking properties, exemplified in figure 4. The figure shows the decay of the spin-locked polarization under the combinations WALTZ17/BLEW12 and WALTZ16E/BLEW12 at $\omega_1 = 100$ kHz for two isochromates of differently oriented

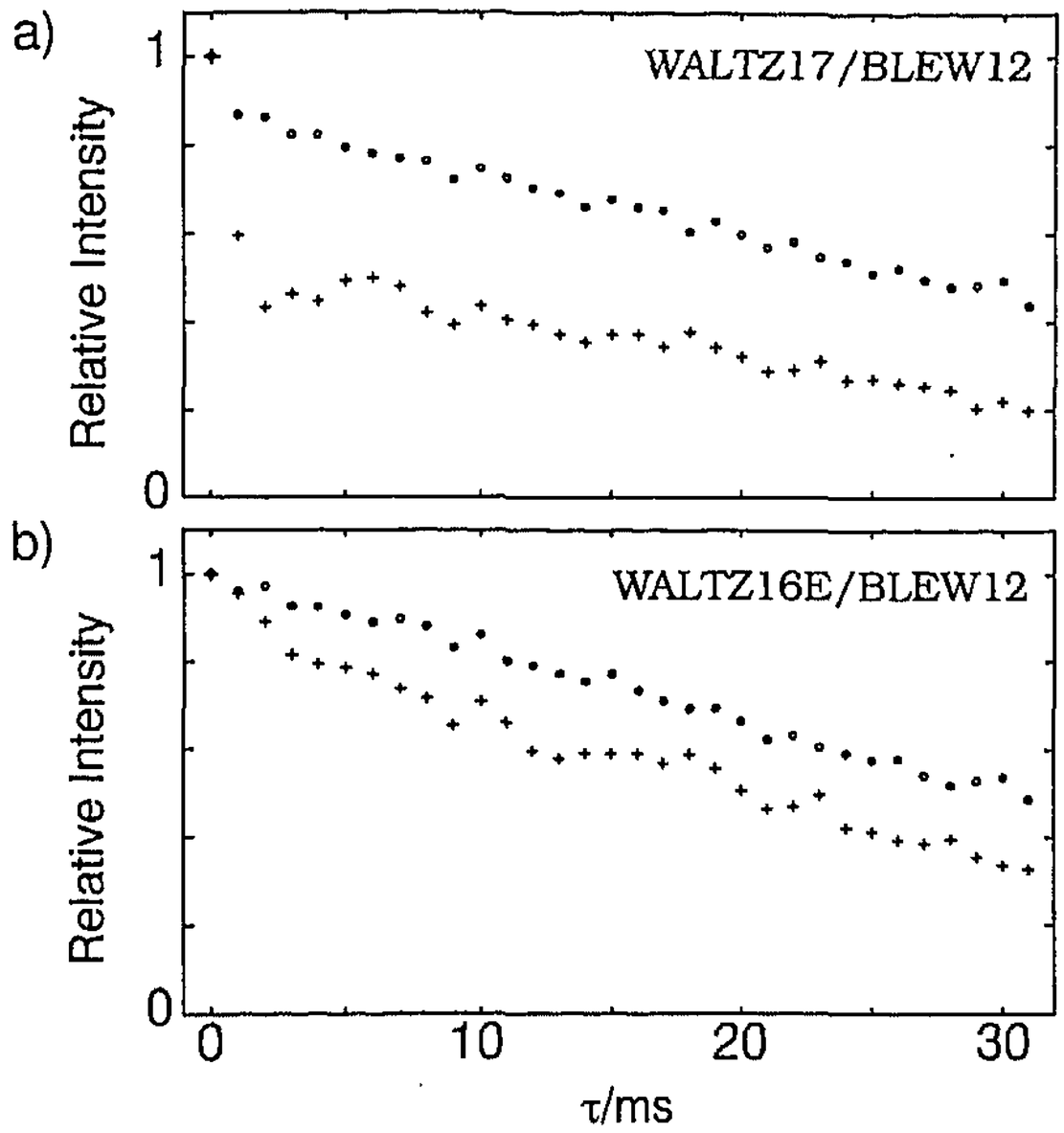

Figure 4. Decay of the polarization of the methoxy carbon in singly ^{13}C-labelled s-PMMA under spin-lock sequences for two orientations of the methyl group in the B_0 field. Crosses are for methyl groups with an axis nearly parallel to the B_0 field. Circles represent methyl groups whose axis is approximately at the magic angle. (*a*) WALTZ17 spin-locking sequence with $\alpha = \pi/2$. (*b*) WALTZ16E sequence where the pulses along $+x$ had an amplitude 2% larger than the ones along the $-x$ direction. Both spin-lock sequences were combined with a BLEW12 irradiation applied to the protons. The amplitudes of the RF fields on the two channels for the $+x$ pulses were 100 kHz.

methoxy groups in singly ^{13}C-labelled syndiotactic poly(methyl methacrylate). Experimental details are given in the next section. For methyl groups whose symmetry axis is close to the magic angle orientation with respect to the static field (circles), both sequences behave equally well because the dipolar I–I interactions are weak (below 2 kHz). On the other hand for methyl groups rotating parallel to B_0 (crosses), the rapid decay of polarization within the first 2 ms, observed with WALTZ17/BLEW12, can be avoided by the use of WALTZ16E/BLEW12. This improvement was also verified with other samples.

4. Experimental

4.1. *Synthesis and characterization of carbon-13 enriched polymers*

Measurements were carried out with polymers selectively labelled with ^{13}C. Atactic and isotactic polystyrene (a-PS and i-PS) were ^{13}C-labelled (^{13}C > 99%) at the carbon atom in the phenyl ring directly bonded to the main chain, referred to as C_1 later on, and ^{13}C-depleted at the methylene group in the main chain. Syndiotactic poly(methyl methacrylate) (s-PMMA) was ^{13}C-labelled at the methoxy group.

4.1.1. *1-(1-^{13}C-Phenyl)-2-^{12}C-ethylene* (*below: 1-^{13}C-β-^{12}C-styrene*)

1-^{13}C-Benzoic acid (^{13}C > 99%) (ICON Services Inc., Summit, NJ, USA) was reduced [31] with $NaAlH_2(OCH_2CH_2OCH_3)_2$ to benzyl alcohol, and the alcohol

oxidized [32] with polymer-bound pyridinium dichromate to benzaldehyde. Styrene was obtained by a Wittig reaction [33] between the aldehyde and the triphenyl phosphonium salt [34] of $^{12}CH_3I$ ($^{12}C > 99{\cdot}9\%$) (Glaser AG, Basel, Switzerland). The overall yield of chemically pure styrene (1-$^{13}C > 99\%$, β-$^{12}C > 99{\cdot}9\%$) was 51%.

4.1.2. *Atactic poly(1-^{13}C-β-^{12}C-styrene)*

1-^{13}C-β-^{12}C-Styrene was polymerized [35] with dibenzoylperoxide at 60 °C for 66 h to atactic poly(1-^{13}C-β-^{12}C-styrene) (1-$^{13}C > 99\%$, β-$^{12}C > 99{\cdot}9\%$) with a yield of 99%. The polymer was purified by repeated dissolution in benzene and precipitation in methanol. It has the characteristics $M_w = 105\,000$, $M_w/M_n = 1{\cdot}7$ (size-exclusion chromatography with detectors for refractive index, viscosity, and light scattering) and $T_g = 95$ °C.

4.1.3. *Isotactic poly(1-^{13}C-β-^{12}C-styrene)*

A supported Ziegler–Natta catalyst of the type $TiCl_4$/ethylbenzoate/$MgCl_2$/$Al(CH_2CH(CH_3)_2)_3$ [36] was used to polymerize 1-^{13}C-β-^{12}C-styrene. After polymerization for 48 h at ambient temperature, poly(1-^{13}C-β-^{12}C-styrene) (1-$^{13}C > 99\%$, β-$^{12}C > 99{\cdot}9\%$) was recovered by precipitation in acidic methanol and washing with methanol. The isotactic polymer was obtained after extraction with methylethylketone (yield 67%). It has the characteristics $M_\eta = 1\,200\,000$ (o-dichlorobenzene, 135 °C), tacticity (m) = 97%, crystallinity about 45% (by X-ray) and $T_m = 220$ °C.

4.1.4. *Syndiotactic poly(^{13}C-methyl methacrylate)*

^{13}C-Methyl methacrylate was prepared by amine-catalyzed reaction of ^{13}C-methanol ($^{13}C > 99\%$) (MSD Isotopes Inc., Montreal, Canada) with methacryloyl chloride [37]. Ion-coordination polymerization initiated with triethylaluminium and $TiCl_4$ in toluene at −78 °C yielded syndiotactic poly(^{13}C-methyl methacrylate) ($^{13}C > 99\%$). The stereoregularity was measured with ^{1}H-NMR to 90% syndiotactic, 9% heterotactic, and 1% isotactic triads. The obtained polymer was amorphous and the molecular weights are: $M_n = 173\,000$, $M_w = 226\,000$ and $M_w/M_n = 1{\cdot}5$.

4.2. *NMR measurements*

The NMR measurements were performed at 295 K on a home-built spectrometer operating at a proton resonance frequency of 220 MHz. The RF-field strengths on both channels of the spectrometer were matched to 100 kHz for all RF-driven polarization-transfer experiments and to 70 kHz for the proton-driven polarization-transfer and for the separated local field experiments.

For the RF-driven measurements in a-PS, the standard WALTZ17/BLEW12 pulse-sequence combination with a 17th pulse corresponding to a $\pi/2$ rotation was used. The $T_{1\rho}$ values of the enriched carbons in a-PS were found to be about 40 ms with variations across the powder pattern below 15%. No difference in the polarization decay was found for the enriched polystyrene sample when comparing WALTZ17/BLEW12 and WALTZ16E/BLEW12. Additional measurements according to the proton-driven pulse scheme (figure 2 (*a*)) at room temperature and at 180 K excluded any contribution from CSA tensor reorientation to the cross-peak intensities when measuring polarization-transfer rate constants at room temperature in singly labelled a-PS.

For methoxy-^{13}C-labelled s-PMMA, the one-bond ^{1}H–^{13}C dipolar interactions introduce a significant orientational dependence of $T_{1\rho}$. In this sample, the WALTZ16E pulse sequence was used with an amplitude of the x-pulses 2% larger than that of the $-x$ pulses. As a result the initial fast decay of the S-spin polarization in the multiexponential $T_{1\rho}$ curve (figure 4) disappeared and an approximately exponential rotating-frame relaxation with time constants of about 33 ms with 25% variations across the powder pattern were observed at a RF-field strength of 100 kHz. This is much longer than the longest mixing time of 5 ms used to evaluate the rate constants. Therefore, significant $T_{1\rho}$ effects on the evaluated polarization-transfer rate constants can be ruled out. As for a-PS, additional measurements according to the proton-driven pulse scheme (figure 2 (*a*)) at room temperature and at 180 K were performed in s-PMMA to exclude any significant contribution from CSA tensor reorientation to the cross-peaks when measuring polarization-transfer rate constants.

5. Quasi-equilibrium polarization-transfer spectra of polystyrenes and s-PMMA

Quasi-equilibrium polarization-transfer spectra, that provide information on the heterogeneity of a sample were obtained using the proton-driven technique. Such spectra could not be recorded by RF-driven polarization transfer because of power-dissipation problems during long mixing times. The differences in transfer rate constants, discussed in the next section, do not affect the quasi-equilibrium state reached after a sufficiently long mixing time.

The 2D polarization-transfer spectrum of a-PS in figure 5 (*a*) was recorded with a mixing time of 10 s within which, based on model calculations, spin diffusion covers a root mean square distance of 50 to 80 Å. The 2D spectrum can be fitted, within experimental error, by a 2D product of the one-dimensional (1D) lineshape function $f(\omega)$ which is given, as an inset, in figure 5 (*a*):

$$f(\omega_1, \omega_2) = f(\omega_1) f(\omega_2). \tag{28}$$

This result shows that a-PS is, averaged over a distance of 50–80 Å, a homogeneous system where all molecular sites and relative orientations of phenyl groups are randomly represented. There are apparently no ordered domains with dimensions exceeding 50–80 Å.

The same features are found for amorphous s-PMMA. A quasi-equilibrium spectrum obtained with a mixing time of 4 s is shown in figure 6. Again it is possible to fit the 2D spectrum by a product of one-dimensional line-shape functions as in equation (28), and there is no orientational order within a sphere of 32 to 50 Å.

To demonstrate the sensitivity to microscopic order, we show in figure 5 (*b*) a polarization-transfer spectrum of semicrystalline i-PS recorded under the same conditions as figure 5 (*a*). It is immediately apparent that this 2D spectrum cannot be the product of two one-dimensional functions. The dominant diagonal ridge indicates that on the experimental time-scale not all spins communicate equally with each other. This is not astonishing since the sizes of the crystallites typically exceed 200 Å in semicrystalline polymers [38]. The ordered domains are thus larger than the distance of 50 to 80 Å over which polarization can diffuse within 10 s. Consequently, the 2D spectrum of figure 5 (*b*) consists of independent and additive contributions from the various crystallites, randomly oriented, and from an amorphous part. Indeed it is possible, as shown in figure 7, to obtain the pure crystalline contributions by

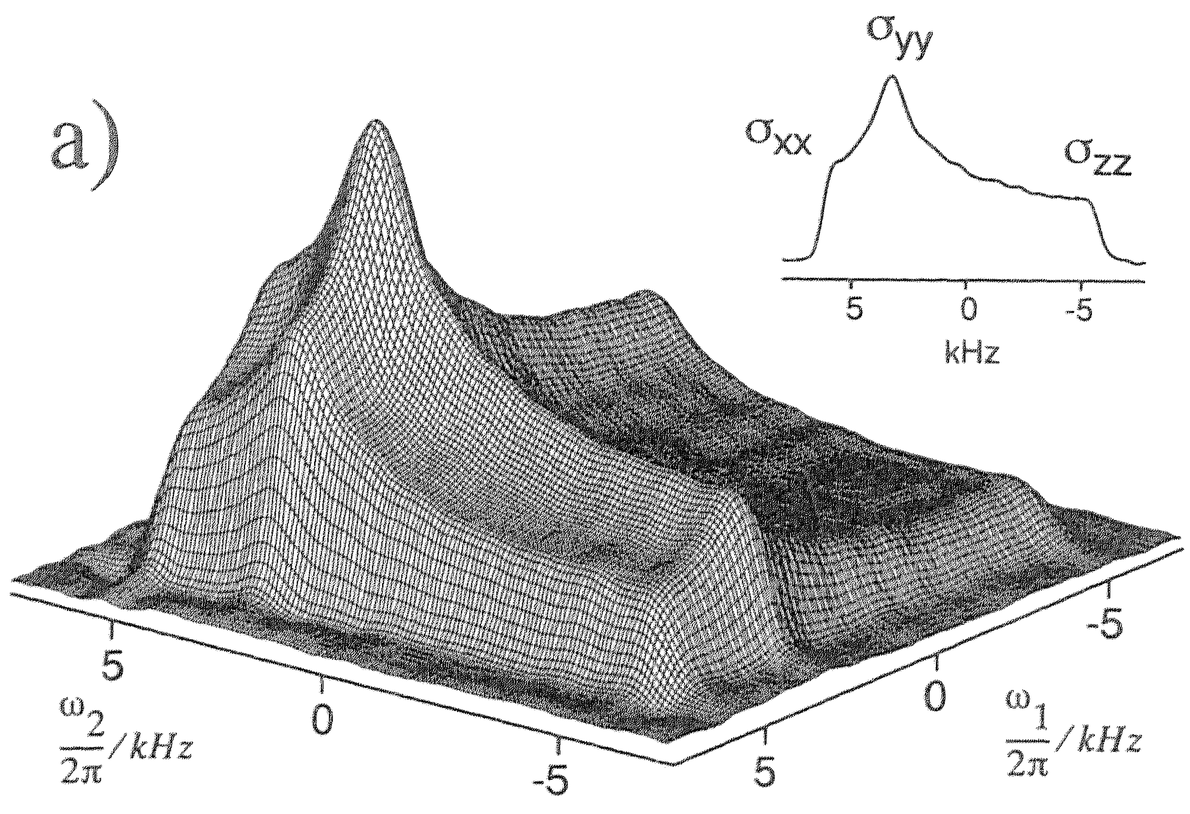

Figure 5. 2D quasi-equilibrium proton-driven polarization-transfer spectra at 295 K of (*a*) amorphous a-PS and (*b*) semi-crystalline i-PS 99% ^{13}C-enriched at the aromatic carbon C_1. The mixing times are in both cases 10 s. The inset in (*a*) represents the 1D powder line-shape of $^{13}C_1$-enriched a-PS.

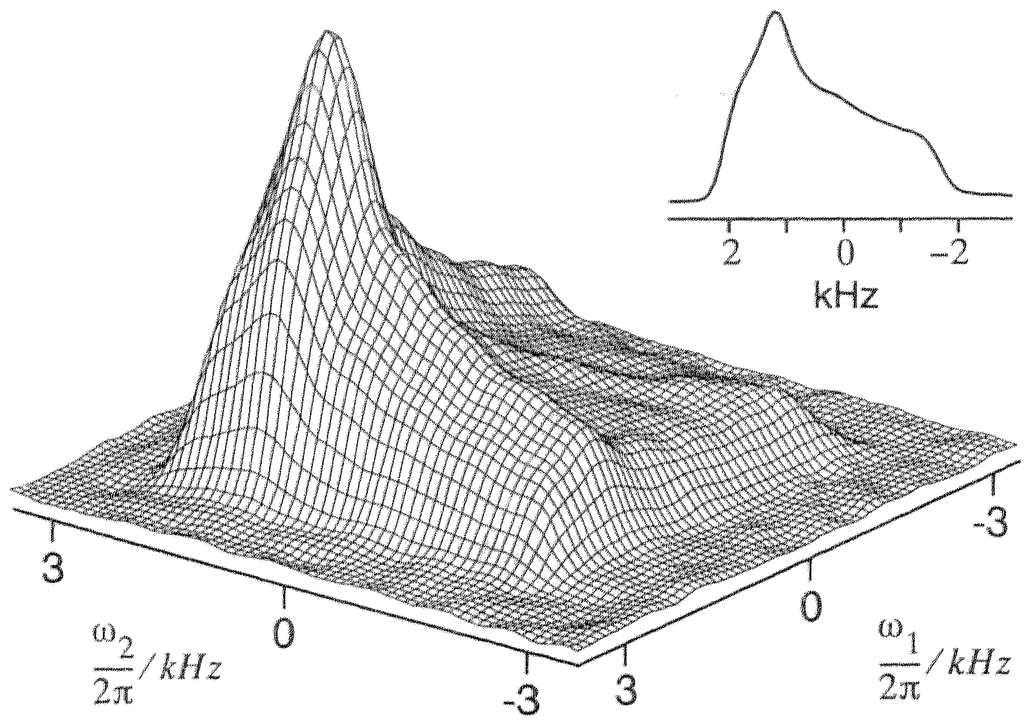

Figure 6. 2D quasi-equilibrium proton-driven polarization-transfer spectrum at 295 K of amorphous s-PMMA 99% ^{13}C-enriched at the methoxy carbon. The mixing time is 4 s. The inset represents the 1D powder line-shape of labelled s-PMMA.

subtracting from figure 5 (*b*) the properly weighted 2D amorphous spectrum of i-PS computed from equation (28). The resulting spectrum of figure 7 (*a*) is nearly identical to the 2D spectrum of figure 7 (*b*) computed according to the structure of crystalline i-PS by Natta *et al.* [39]. The isosterism postulated therein was neglected, and the

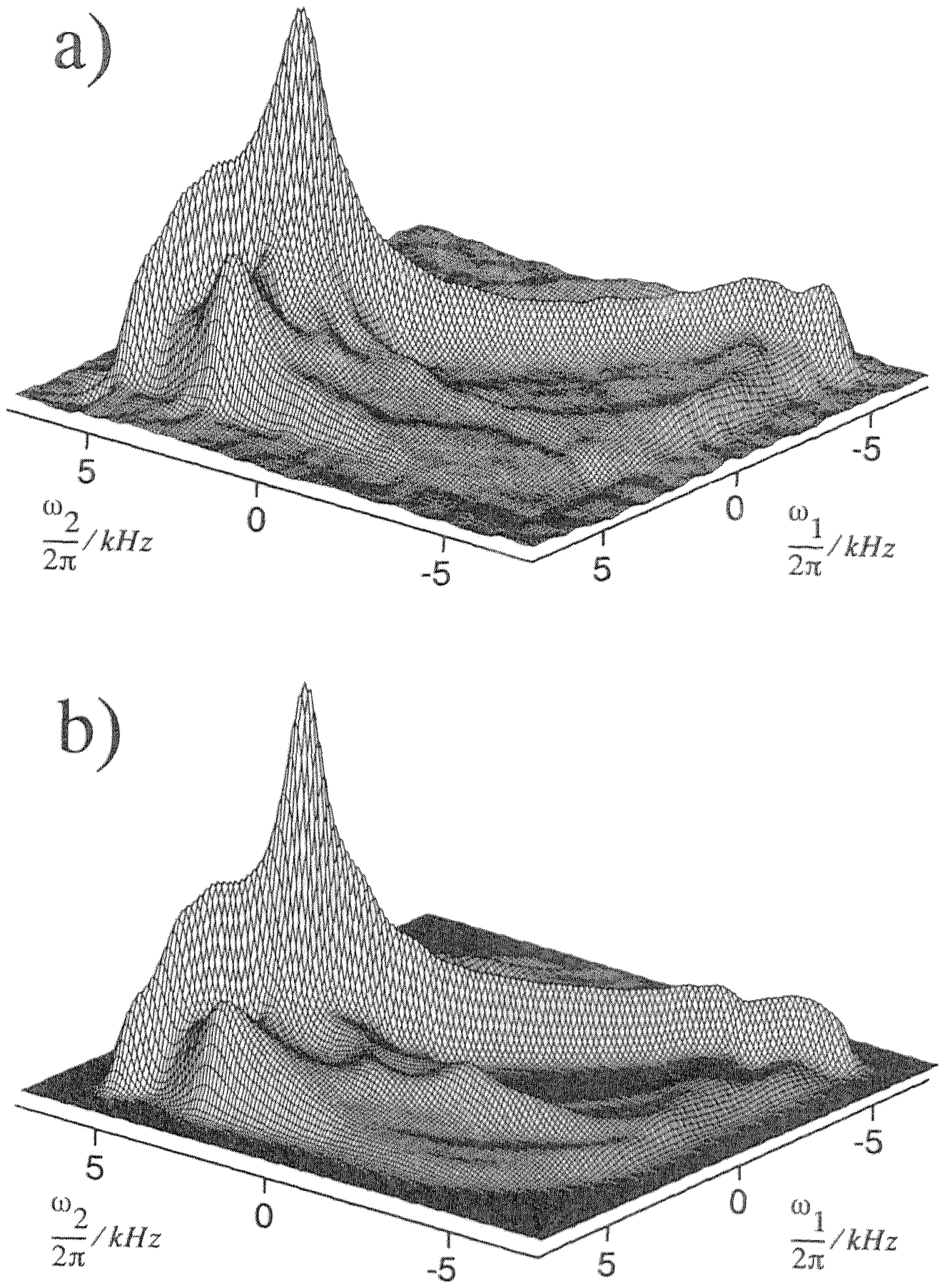

Figure 7. (*a*) Experimental and (*b*) computed 2D quasi-equilibrium polarization-transfer spectra of the crystalline part of i-PS. The experimental data were obtained by subtracting a 60% contribution of amorphous i-PS from the spectra of figure 5 (*b*). The amorphous contribution was computed according to equation (28). The amplitude of the subtracted amorphous part was increased until the intensity in the central part of the difference spectrum, where no signal is expected according to the computed spectrum of figure 7 (*b*), vanished. The computed spectrum (*b*) was obtained by using the coordinates published in [39] and assuming that the orientation of the CSA tensor of the labelled site conforms to the symmetry of the phenyl ring (see text). The eigenvalues of the CSA tensor were obtained by a fit to a 1D spectrum ($\nu_{XX} = 6100$ Hz, $\nu_{YY} = 3220$ Hz and $\nu_{ZZ} = -6100$ Hz or $\delta_{XX} = 237$ p.p.m., $\delta_{YY} = 183$ p.p.m. and $\delta_{ZZ} = 17$ p.p.m. from TMS). The 2D line-shape was assumed to be Gaussian with a full width at half height of 600 Hz.

orientation of aromatic carbon CSA tensor was assumed to be determined by the symmetry of the side group. The most shielded axis of the CSA tensor is perpendicular to the plane of the phenyl ring and the direction of the least shielded axis coincides with the direction of the bond to the main chain [1]. The good agreement between the measured and the computed data supports the reliability of the NMR method.

6. Polarization-transfer rate constants and geometrical rate factors in amorphous a-PS and s-PMMA

The measurement of polarization-transfer rate constants and geometrical rate factors in amorphous polymers is of interest for the detection of local order whose presence is difficult to verify with other techniques, and for the experimental test of

computer model simulations. At first, the offset dependence of the rate constants is discussed. It could adversely affect the significance of the experimental results.

6.1. *Experimental offset dependence of the RF-driven polarization-transfer rate constants*

The offset dependence of the rate constants W_{ij} for the RF-driven polarization transfer is given by the scaled chemical shielding difference and the dipolar scaling factor both plotted in figure 3. To test this dependence, we measured five 2D polarization-transfer spectra for a-PS with the RF carrier positioned at an offset of 0, 2, 4, 6, and 10 kHz from the centre frequency of the ^{13}C powder pattern that spreads over ± 6 kHz. The mixing time of 7 ms ensures that the cross-peak intensities are still in the initial rate regime. The intensities were measured at four locations *a*, *b*, *c*, and *d* within the 2D spectra for all five offsets of the RF carrier. This leads to the four offset dependence plots shown in figure 8.

The theoretical offset dependence was computed from equation (17) with the values of figure 3. The line-shape function of the ZQ spectrum was assumed to be Gaussian with a full width at half height of 160 Hz as estimated from the homogeneous width of the proton-decoupled ^{13}C spectrum. For each of the graphs *a*, *b*, *c*, and *d* the maximum value is normalized to 1, and there is no absolute relation between them. The survey plot of figure 8 (*e*) shows that the strongest offset dependence is parallel to the main diagonal.

For the graphs *a* and *b* that monitor the offset dependence near the main diagonal the agreement between experiment and calculation is good. However, there is a stronger experimental offset dependence in the graphs *c* and *d* that are further away from the diagonal. It could be attributed to an overestimate of the width of the ZQ transition. In any case, the variation within the offset range of ± 6 kHz used in the 2D plots of this paper, and identical to the grey square in figure 8 (*e*), is less than 10%. This implies that for the RF-driven polarization transfer the polarization-transfer rate constants are a direct measure for the geometrical rate factors as mentioned already in section 3.2.

6.2. *Spectral factors of the proton-driven polarization-transfer rate constants*

In contrast to the RF-driven polarization transfer, the evaluation of geometrical rate factors from the rate constants of proton-driven polarization transfer must take into account the dependence of $F^H_{AB}(0)$ on (Ω_A, Ω_B). In the absence of a direct measure for the ZQ line-shape function, it is necessary to estimate it based on equation (21). The single-quantum line-shape functions $f^H_A(\omega)$ and $f^H_B(\omega)$ are extracted as sections along ω_1 at $\omega_2 = \Omega_A$ and Ω_B, respectively, from the separated local field spectra [40] of figure 9. The spectra were recorded in the absence of decoupling during the evolution period.

For the $^{13}C_1$-enriched a-PS, all sections along ω_1 of the separated local field spectrum of figure 9 (*a*) are singlets. The full width at half height of the nearly Gaussian sections varies within $5{\cdot}6 \pm 1{\cdot}4$ kHz. The reason for this moderate variation is the absence of directly bonded protons and a rather isotropic distribution of the nearest neighbours. Assuming uncorrelated broadening mechanisms, this leads to a ZQ line-width larger by a factor of $\sqrt{2}$, amounting to $7{\cdot}9 \pm 2{\cdot}0$ kHz. It should be mentioned that this estimation disregards the fact that the sections through

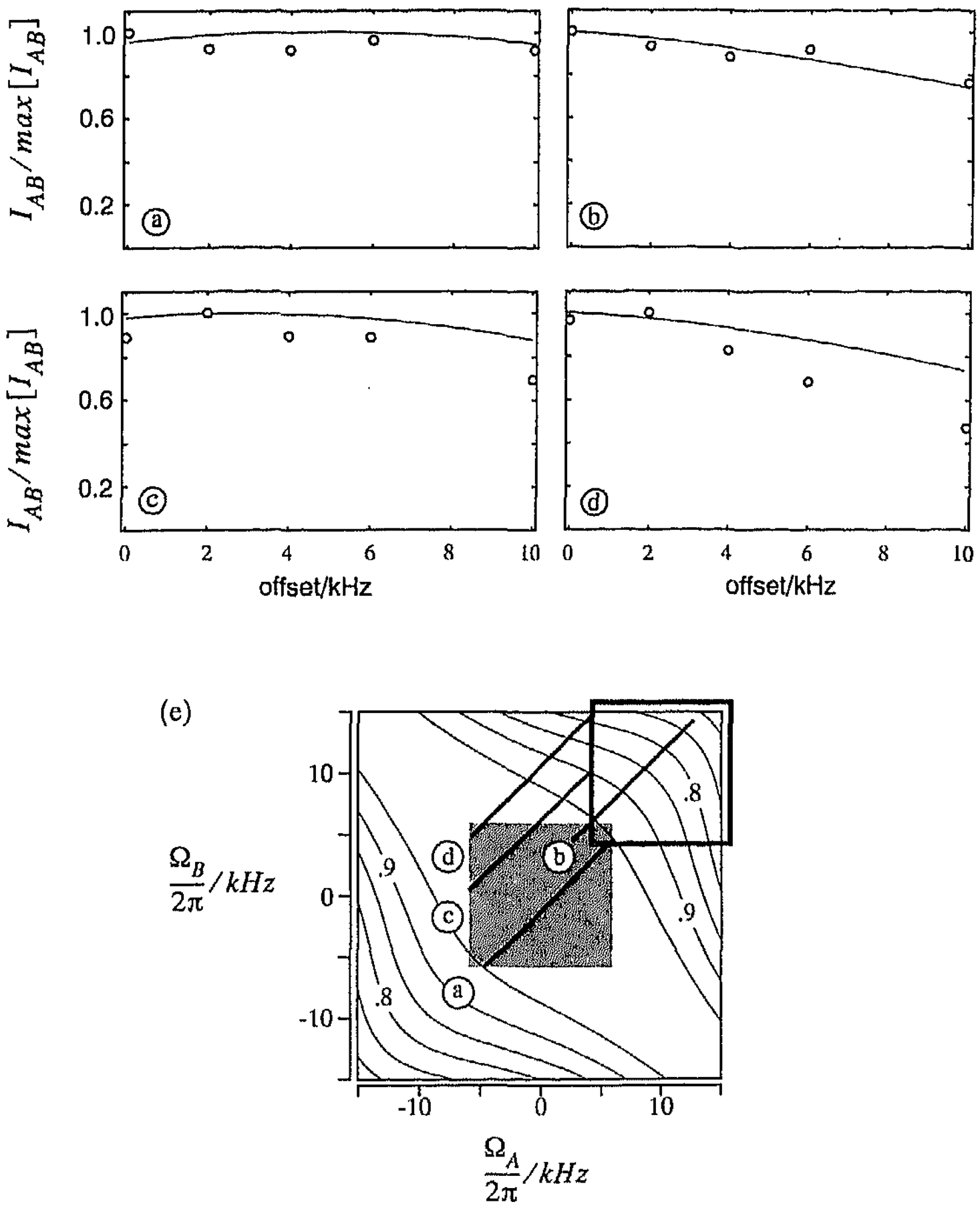

Figure 8. Frequency dependence of the cross-peak intensity for RF-driven polarization transfer under a WALTZ17 pulse sequence. The relative cross-peak intensities $I_{AB}/\max[I_{AB}]$ measured in a-PS are given by the circles. The corresponding theoretical values in the initial rate regime $s_{AB}^2 F_{AB}^{rf}(0)/\max[s_{AB}^2 F_{AB}^{rf}(0)]$ are given by the curves. In (*a*)–(*d*) the intensities are plotted as functions of the RF-carrier frequency offset from the centre of the powder pattern. At offset zero, the 2D spin-diffusion spectrum of a-PS covers the grey area in (*e*). The grey square in (*e*) indicates the region covered by the a-PS spectrum for a carrier offset of 10 kHz. The experimental points were recorded for offsets 0, 2, 4, 6, and 10 kHz. The measured points in (*a*)–(*d*) lie on the respective traces indicated in (*e*). The theoretical curves are computed from the data of figure 3 for a uniform ZQ spectrum whose full width at half height is 160 Hz. The contours in the survey plot (*e*) indicate $s_{AB}^2 F_{AB}^{rf}(0)/\max[s_{AB}^2 F_{AB}^{rf}(0)]$. At $\Omega_A = \Omega_B = 0$, this factor is 1.

figure 9 (*a*) may consist of superimposed lines with different widths. A model calculation based on isotactic trans–trans diads with phenyl groups perpendicular to the chain axis shows that the line-width variation is less than 10% within a given isochromate. The dependence of the computed values $F_{AB}^{H}(0)$ on Ω_A and Ω_B is shown in figure 10 (*a*). It is obvious that the strong offset dependence requires a resonance-frequency-dependent correction of the experimental rate constants before their interpretation in terms of order.

The situation for amorphous ^{13}C-methoxy-labelled s-PMMA is different insofar as the separated local field spectrum of figure 9 (*b*) shows for several sections along

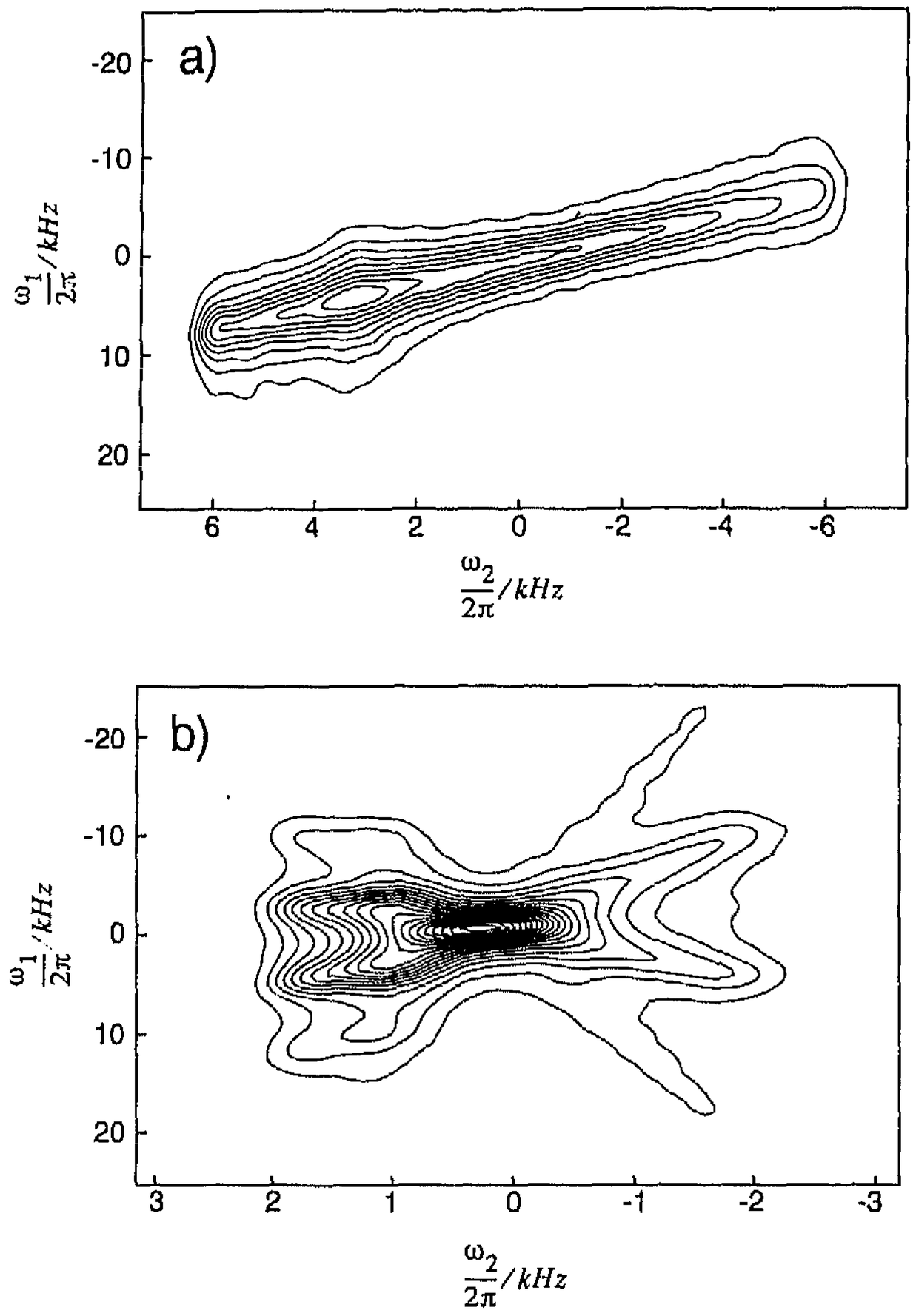

Figure 9. Contour plot of the separated local field spectra of the ^{13}C-labelled a-PS (*a*) and s-PMMA (*b*). The chemical shielding-resolved single-quantum line-shapes under coupling to the protons can be obtained from sections along ω_1. For s-PMMA, the quartet splitting along ω_1 is due to the dominating heteronuclear dipolar interactions with the three methyl protons.

ω_1 a clear quartet structure due to the three methyl protons. The quartet splitting strongly depends on the chemical shielding position because of the nearly coaxial dipolar and CSA tensors. The same treatment as for a-PS leads to the offset dependence of $F^H_{AB}(0)$ shown in figure 10 (*b*). It is qualitatively similar to figure 10 (*a*), taking into account the smaller frequency range in figure 10 (*b*).

6.3. *Discussion of the geometrical rate factors in a-PS and s-PMMA*

Based on proton-driven and RF-driven polarization-transfer spectra of amorphous a-PS with mixing times from 1 to 50 ms and 0·5 to 4 ms, respectively, the rate constants, shown in figure 11 (*a*) and (*c*), were evaluated in the initial rate regime as functions of the offset frequencies Ω_A and Ω_B. A comparison of the resulting geometrical rate factors from (*a*) the proton-driven rate constants with (*c*) the RF-driven ones is also given in figure 11. The comparison is limited to a slice parallel to the diagonal in the 2D spectrum because of large experimental errors outside of this range for the proton-driven data. From the RF-driven rate constants, the

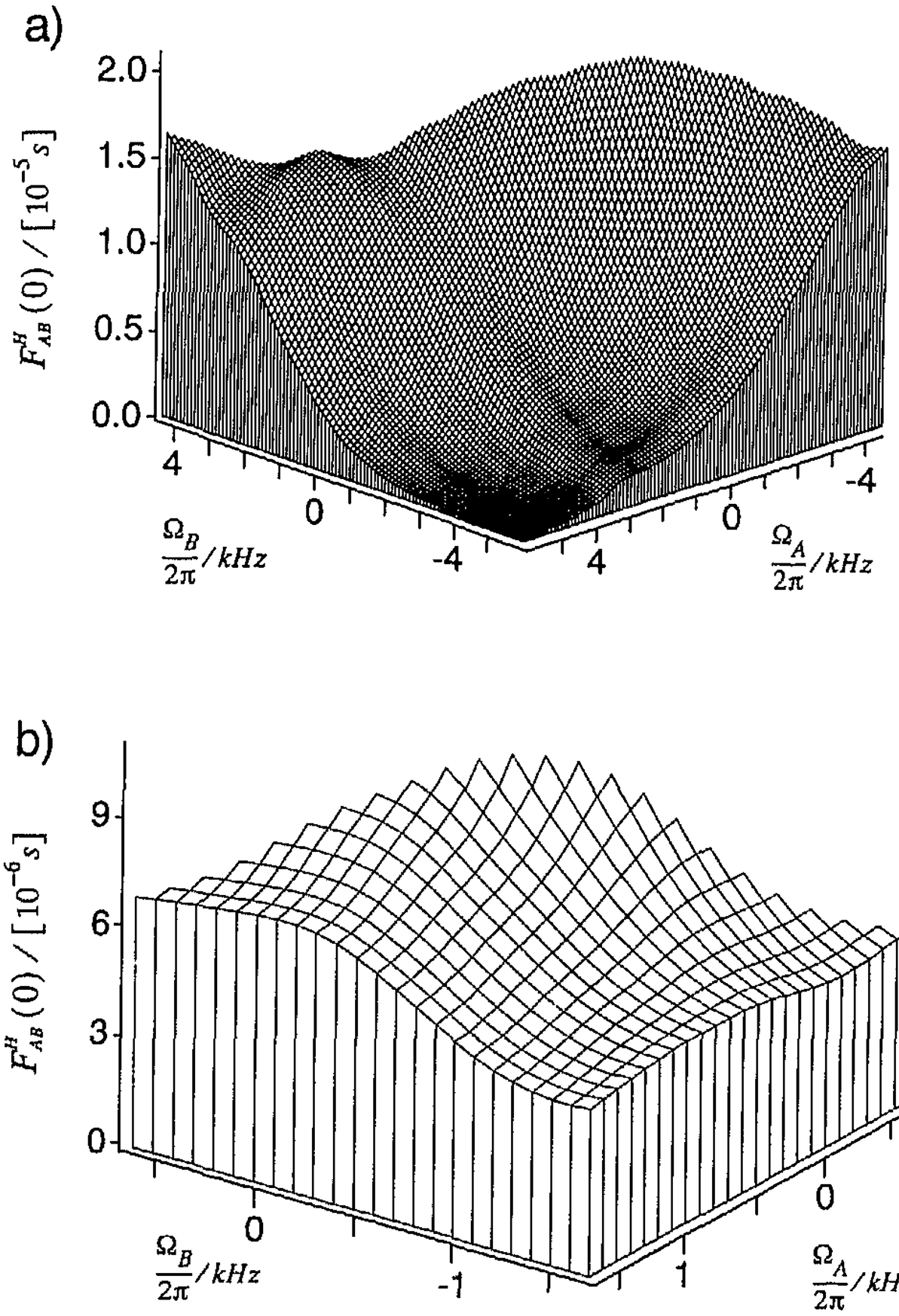

Figure 10. Intensity of the ZQ spectrum at frequency zero for a pair of ^{13}C-labelled carbon isochromates under coupling to the protons for the cross-peak region of (*a*) amorphous a-PS and (*b*) s-PMMA. $F^H_{AB}(0)$ was computed from equation (21). The 1Q spectra $f^H_A(\omega)$ and $f^H_B(\omega)$ were extracted from the corresponding 2D experiments of figure 9 along ω_1 at $\omega_2 = \Omega_A$ and $\omega_2 = \Omega_B$.

geometrical rate factors are easily evaluated from equation (17) using the experimentally determined value of $F^{\mathrm{rf}}_{AB}(0) = 8{\cdot}4 \times 10^{-4}$ s. Here g_{AB} has the same offset dependence as R^{rf}_{AB} and is also given in figure 11 (*c*) using the second scale. The geometrical rate factors extracted from R^H_{AB} by division by $F^H_{AB}(0)$ of figure 10 (*a*) and the appropriate scaling factor (equation (17)) are given in figure 11 (*b*). This correction of the rate constants reduces the incline both along and perpendicular to the main diagonal of the profile of figure 11 (*a*), as far as it is due to the offset dependence of $F^H_{AB}(0)$. It leads to a geometrical rate-factor profile that matches well the one of the RF-driven transfer in figure 11 (*c*).

The rate constants and the geometrical rate factors from the RF-driven experiments are shown over the full frequency range in figure 12 (*a*). The highest values are found along the diagonal and, in particular, on the low-frequency side corresponding to $^{13}C_1$ nuclei in phenyl-ring planes oriented perpendicularly to the external field. For this orientation, the principal axis associated with the most shielded principal value of the CSA tensor is aligned, approximately, with the external field.

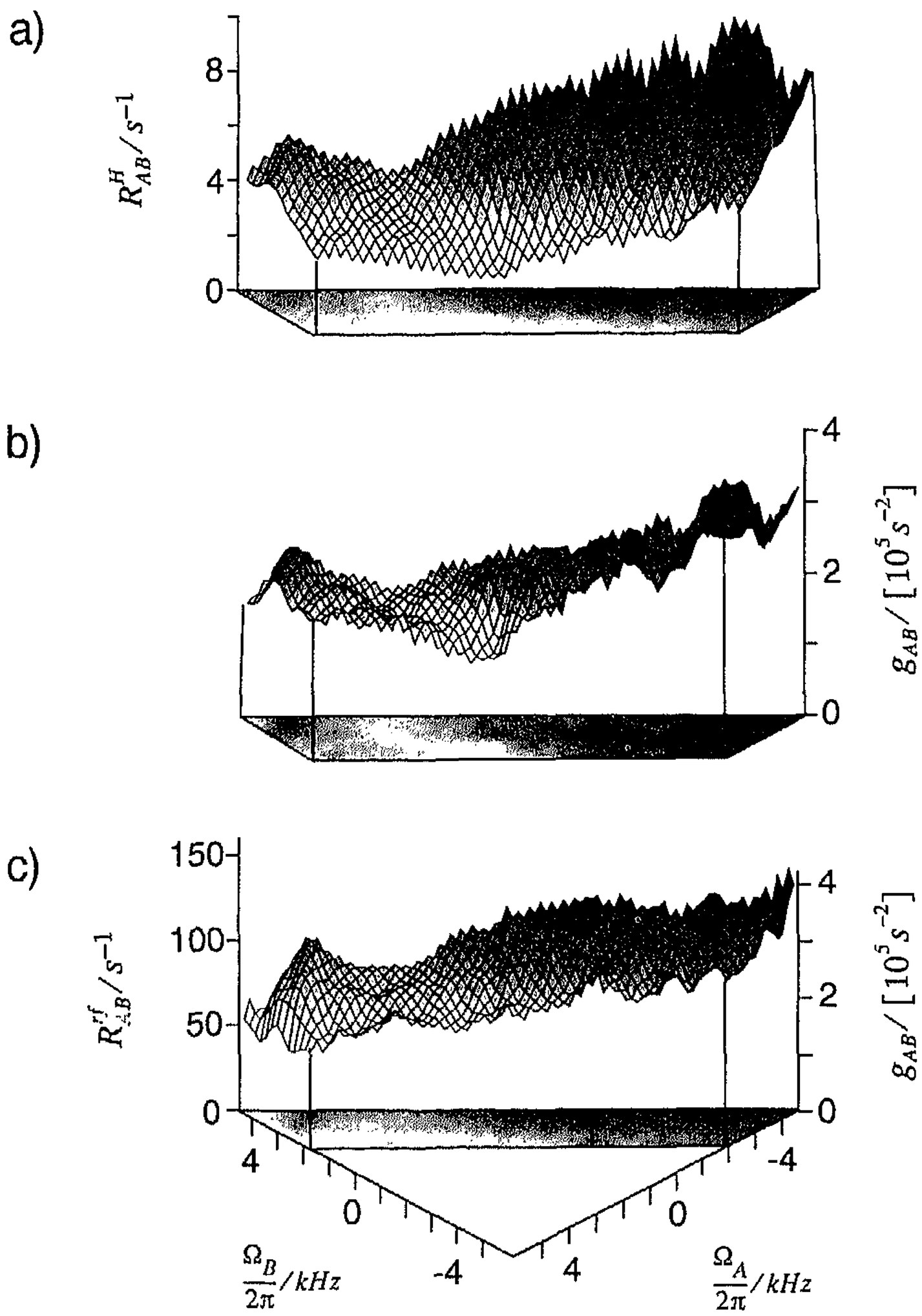

Figure 11. (*a*) Rate constants of proton-driven polarization transfer for part of the cross-peak region of amorphous ^{13}C-labelled a-PS. The rate constants were measured in the initial rate approximation for ten mixing times up to 50 ms. (*b*) Geometrical rate factors obtained from the rate constants in (*a*) according to equation (17). $s_{AB} = 1$ and the corresponding spectra rate factors $F^H_{AB}(0)$ are taken from the data presented in figure 10 (*a*). (*c*) Rate constants of RF-driven polarization transfer under WALTZ17/BLEW12 irradiation in ^{13}C-labelled a-PS measured in the initial rate approximation with eight mixing times up to 4 ms. The second scale indicates the geometrical rate factors obtained from R^{rf}_{AB} according to equation (17) using $s_{AB} = -1/2$ and $F^{rf}_{AB}(0) = F^{rf}(0) = 8{\cdot}4 \times 10^{-4}$ s. The displayed frequency range is restricted to the same domain as in (*a*) to ease the comparison. In the ground plane, a density plot is given to facilitate the interpretation of the 3D plots.

The observed enhanced transfer rates between rings that are both oriented perpendicularly to the external field direction can be caused either by the distance dependence (r_{ij}^{-6}) or the angular dependence ($3\cos^2\theta_{ij} - 1$) of the dipolar coupling frequency and we cannot unambiguously determine the individual contribution of these terms to the observed variations of the coupling frequency. The disc-like geometry of the phenyl rings suggests that two rings that approach each other closely are nearly parallel with θ_{ij} values much smaller than 90°. Both contributions can explain the observed short-range order in figure 12. For larger inter-ring distances, the

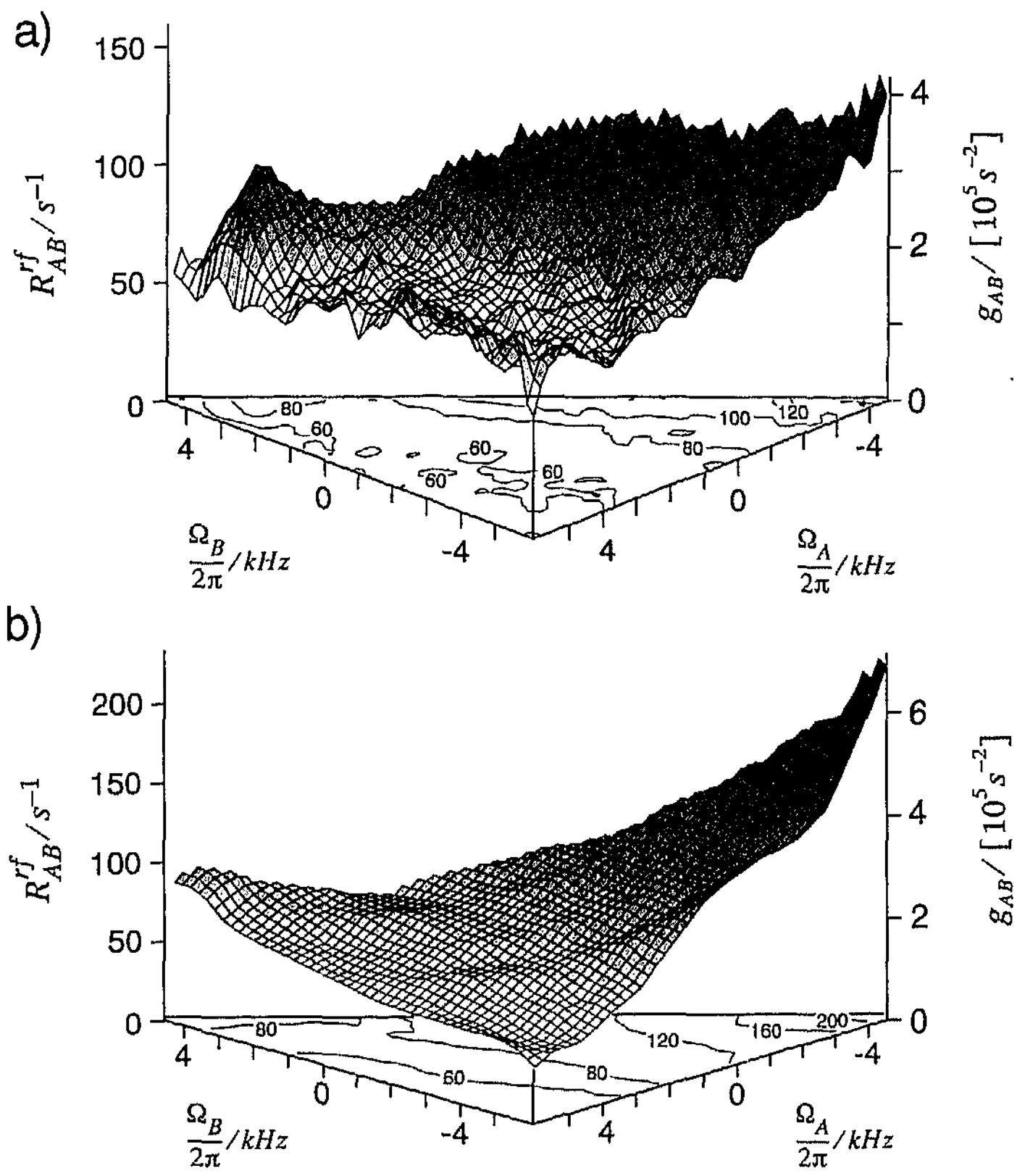

Figure 12. (*a*) Rate constants of RF-driven polarization transfer under WALTZ17/BLEW12 irradiation in ^{13}C-labelled a-PS measured in the initial rate approximation with mixing times up to 4 ms. The plot extends the data shown in figure 11 (*c*) and covers the full cross-peak area. The second scale indicates the corresponding geometrical rate factors obtained from R^{rf}_{AB} according to equation (17) using $s_{AB} = -1/2$ and $F^{rf}_{AB}(0) = F^{rf}(0) = 8{\cdot}4 \times 10^{-4}$ s. (*b*) Polarization-transfer rate constants and geometrical rate factors computed from the a-PS microstructure that best agree with the experimental values displayed in (*a*). The data were averaged over 15 structures obtained in a molecular dynamic simulation of that microstructure. The rate constants are computed according to equation (17) using the same parameters s_{AB} and $F^{rf}(0)$ as in (*a*).

importance of the angular term is expected to decrease. A more specific explanation requires detailed modelling of amorphous atactic polystyrene (a-PS).

To obtain more insight into local ordering, computer simulations of amorphous a-PS have been undertaken which will be described in more detailed elsewhere [41]. Twenty four microstructures of a-PS, constructed by Rapold *et al.* [42] containing 40 monomer units of a-PS, were submitted to 500 steps energy minimization and to a 25 ps molecular dynamics procedure to obtain low energy conformations. They were analysed in terms of the relative orientation of the phenyl groups and the C_1–C_1 distances. Hypothetical profiles of geometrical rate factors that could be compared with figure 12 (*a*) were computed and averaged for each microstructure over the last 3/5 of a 25 ps molecular dynamics run. The microstructure whose profile best agreed with the experimental results was selected.

The weighted distribution of the angle β between two phenyl planes for given ranges of C_1–C_1 distances extracted from the selected microstructure is shown in figure 13. In the distance interval 3–4 Å low angles dominate, indicating a preference for nearly parallel rings at short distances. For the intervals 4–5 Å and 5–6 Å already a virtually isotropic arrangement exists.

The profile of geometrical rate factors of the selected microstructure is displayed in figure 12 (*b*). It exhibits features remarkably similar to the experimental data of figure 12 (*a*). The same trend of the intensities, increasing towards the diagonal and towards the low-frequency side, is visible. Apparently the computed distribution, characterized in figure 13, represents the experimental situation well. It can thus be concluded that a significant orientational correlation among the phenyl groups exists within a distance range of 3–4 Å. Most of the phenyl pairs, whose C_1–C_1 distances are less than 4 Å, belong to neighbouring monomer units. However, it is not clear whether the ordering is exclusively caused by geometric properties of the phenyl groups determining the distance of closest approach or whether there is an ordering mechanism that goes beyond this geometrical effect. Assuming that the order in amorphous a-PS decays with increasing distance the NMR data also support the absence of orientational correlation between rings that are more than 5 Å apart. These results do not agree with previous structural investigations in atactic polystyrene with wide-angle X-ray [43] and wide-angle neutron scattering [44, 45]. In the X-ray study, supramolecular structures were postulated with stacking of the phenyl rings over 15 Å, whereas the results from neutron diffraction were interpreted in terms of paracrystallinity with a grain size of 20 Å.

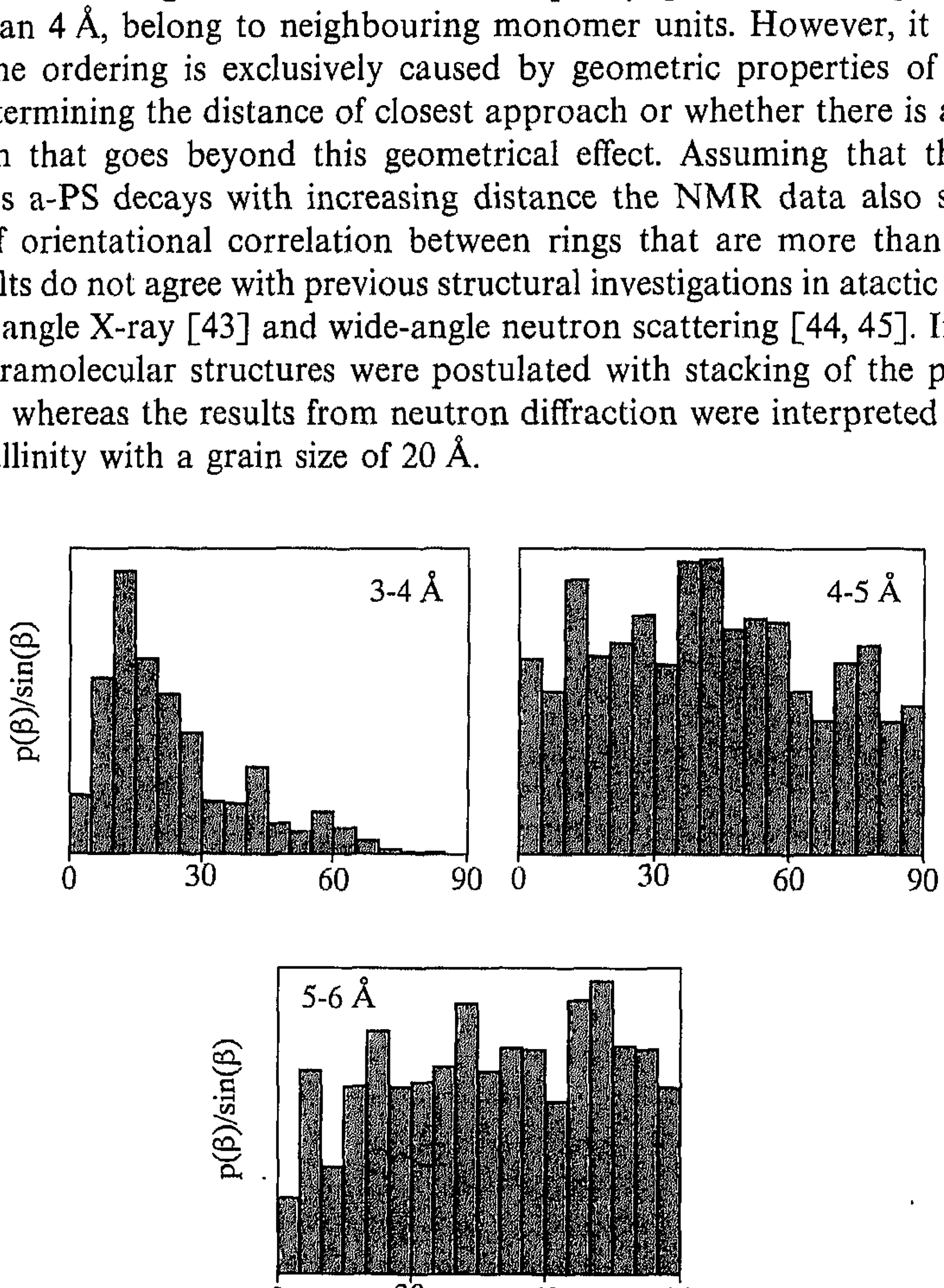

Figure 13. Weighted distribution $p(\beta)/\sin(\beta)$ of the angle β between two phenyl planes as a function of the distance between the two C_1 carbons. The considered distance interval appears in the respective plot. The distributions were calculated from 15 time frames taken from the molecular dynamics simulation of the microstructure whose profile of geometrical rate factors best agrees with the experimental values displayed in figure 12 (*a*).

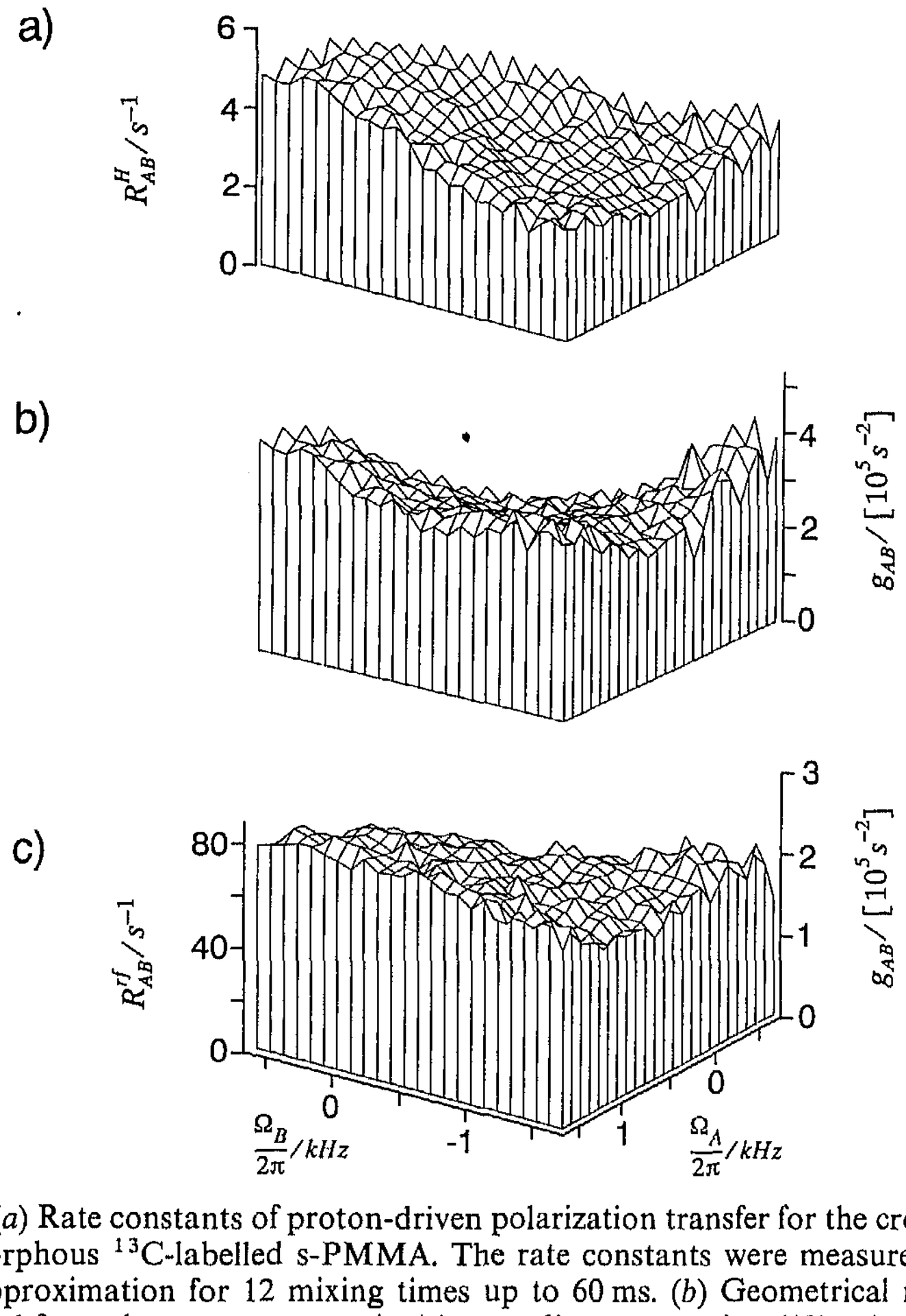

Figure 14. (*a*) Rate constants of proton-driven polarization transfer for the cross-peak region of amorphous ^{13}C-labelled s-PMMA. The rate constants were measured in the initial rate approximation for 12 mixing times up to 60 ms. (*b*) Geometrical rate factors are obtained from the rate constants in (*a*) according to equation (17). The dipolar scaling factor is set to $s_{AB} = 1$, and the corresponding spectral rate factors $F^H_{AB}(0)$ are taken from the data presented in figure 10 (*b*). (*c*) Rate constants of RF-driven polarization transfer under WALTZ16E/ BLEW12 irradiation measured in the initial rate approximation with ten mixing times up to 5 ms. The amplitude of the x pulses was set 2% higher than the one of the $-x$ pulses. The RF amplitude for the stronger pulses was 100 kHz. The scale on the right indicates the geometrical rate factors obtained from R^{rf}_{AB} according to equation (17) using $s_{AB} = -1/2$ and $F^{rf}_{AB}(0) = F^{rf}(0) = 7{\cdot}9 \times 10^{-4}$ s.

An analogous investigation of local order in s-PMMA is documented in figure 14. The geometrical rate factors from the RF-driven polarization transfer in figure 14 (*c*) show only a minor offset dependence along the main diagonal with a 20% increase from the low frequency to the high frequency end. A similar variation is also visible in the geometrical rate factors obtained from proton-driven transfer rate constants (figure 14 (*b*)) although artifacts from an imperfect offset correction of the raw rate constants by $F^H_{AB}(0)$ might be present. An insufficient correction seems to appear for large offsets in the 2D profile, leading to g_{AB} values larger than the ones in figure 14 (*c*). It is unlikely that the 20% variation of the geometrical rate factors in figure 14 (*c*) is an experimental artifact. Neither the variations of $T_{1\rho}$ with the offset nor a variation of the homonuclear ^{13}C line-width can explain it. The $T_{1\rho}$ values

vary by 25% but their effect is negligible as they exceed the longest mixing time of 5 ms by at least a factor of five. The average single-quantum transition dipolar line-width is 240 Hz (full width at half height) and the variations are smaller than 8% with an incorrect tendency. It is therefore likely that the slight slope in the geometrical rate-factor profile indicates indeed a weak ordering effect reflected in a variation of the average dipolar coupling between two methoxy carbons with different relative orientations of the methyl group axes. A distance variation as small as 3% could explain the observed 20% variation of the geometrical rate factors.

7. Conclusions

Two-dimensional polarization-transfer experiments for static samples can yield information on structure and order in crystalline, semicrystalline, and most interestingly in amorphous solids. It is possible to measure either polarization-transfer rate constants in the initial rate regime to observe short-range order on a molecular scale up to a few Angstroms, or to record quasi-equilibrium spectra for monitoring heterogeneity and to characterize long-range order within a range of about 100 Å.

For measurements of polarization-transfer rate constants, the RF-driven polarization-transfer experiment is to be preferred. It provides, without requiring any critical corrections of the data, access to the geometrical rate factors that can characterize spatial order. The proton-driven transfer rate constants, on the other hand, are susceptible to undesired frequency-offset effects and to an orientation-dependent dipolar line-width of the zero-quantum transition. Then, a frequency-dependent correction of the rate constants has to precede the evaluation of local order.

Only proton-driven polarization transfer is suitable for the measurement of quasi-equilibrium ^{13}C polarization-transfer spectra. Power-dissipation problems during the required mixing times, generally up to a few hundreds of milliseconds, preclude the application of strong RF fields necessary for RF-driven polarization transfer. The mentioned variations of the transfer-rate constants under proton-driven conditions are not of much relevance for recording quasi-equilibrium spectra.

The experiments on amorphous samples of a-PS and s-PMMA have shown that in both samples there is little local ordering. A comparison with computer simulations allows us to quantify a relation between orientational order and minimum distance of phenyl rings in a-PS. The comparison also supports the view that the orientational correlation does not extend beyond about 5 Å. The evaluated short-range ordering may possibly be explained by the disc-like geometry of the phenyl rings themselves. In the absence of a detailed structural model, local ordering among the methoxy groups in amorphous s-PMMA could not be quantified.

The study shows that structural information on amorphous samples is contained in NMR polarization-transfer data, and it is possible to detect the presence or absence of molecular order in a range of about 100 Å. The quantitative evaluation of order parameters in partially ordered systems, however, requires extensive atomistic modelling. NMR provides then a sensitive test for accepting or rejecting structural and molecular models.

We are indebted to Dr Bernhard Glomm for determining the crystallinity of the isotactic polystyrene and to Marcel Zehnder for his help with the molecular models. We would also like to thank Dr M. Galimberti (Himont, Ferrara, Italy) for generously providing the catalyst used to prepare the isotactic polystyrene and Dr K. Bouchal,

Dr P. Vlaek and Dr J. Spevacek (Institute of Macromolecular Chemistry, Prague, Czech Republic) for the synthesis and characterization of s-PMMA. This work has been supported by the Swiss National Science Foundation and by the Aluminium Fonds, Neuhausen.

References

[1] MEHRING, M., 1983, *High Resolution NMR in Solids* (Heidelberg: Springer).
[2] GRIFFITHS, J. M., and GRIFFIN, R. G., 1993, *Analytica chim. Acta*, **283,** 1081.
[3] ABRAGAM, A., 1961, *The Principles of Nuclear Magnetism* (Oxford: Clarendon).
[4] BLOEMBERGEN, N., 1949, *Physica*, **15,** 389.
[5] ASSINK, R. A., 1978, *Macromolecules*, **11,** 1233.
[6] VIRLET, J., and GHESQUIRES, D., 1980, *Chem. Phys. Lett.*, **73,** 323.
[7] CARAVATTI, P., DELI, J. A., BODENHAUSEN, G., and ERNST, R. R., 1982, *J. Am. chem. Soc.*, **104,** 5506.
[8] TYCKO, R., and DABBAGH, G., 1991, *J. Am. chem. Soc.*, **113,** 3592.
[9] TYCKO, R., and DABBAGH, G., 1991, *Mater. Res. Soc. Symp. Proc.*, **215,** 125; 1992, *Israel J. Chem.*, **32,** 179.
[10] DABBAGH, G., WELIKY, D. P., and TYCKO, R., 1994, *Macromolecules*, **27,** 6183.
[11] ROBYR, P., MEIER, B. H., and ERNST, R. R., 1991, *Chem. Phys. Lett.*, **187,** 471.
[12] ROBYR, P., MEIER, B. H., FISCHER, P., and ERNST, R. R., 1994, *J. Am. chem. Soc.*, **116,** 5315.
[13] MITCHELL, G. R., 1989, *Comprehensive Polymer Science* (Oxford: Pergamon), Vol. 1 chap. 31.
[14] ERNST, R. R., BODENHAUSEN, G., and WOKAUN, A., 1987, *Principles of Nuclear Magnetic Resonance in One and Two Dimensions* (Oxford: Clarendon).
[15] EDZES, H. T., and BERNARDS, J. P. C., 1984, *J. Am. chem. Soc.*, **106,** 1515.
[16] HENRICHS, P. M., and LINDER, M., 1984, *J. magn. Reson.*, **58,** 458.
[17] CARAVATTI, P., NEUENSCHWANDER, P., and ERNST, R. R., 1985, *Macromolecules*, **18,** 119.
[18] MEIER, B. H., 1994, *Adv. magn. opt. Reson.*, **18,** 1.
[19] ROBYR, P., MEIER, B. H., and ERNST, R. R., 1989, *Chem. Phys. Lett.*, **162,** 417.
[20] TOMASELLI, M., MEIER, B. H., BALDUS, M., EISENEGGER, J., and ERNST, R. R., 1994, *Chem. Phys. Lett.*, **225,** 131.
[21] SUTER, D., and ERNST, R. R., 1985, *Phys. Rev.* B, **32,** 608.
[22] VANDERHART, D. L., 1987, *J. magn. Reson.*, **72,** 13.
[23] HENRICHS, P. M., LINDER, M., and HEWITT, J. M., 1986, *J. chem. Phys.*, **85,** 7077.
[24] KUBO, A., and MCDOWELL, C. A., 1988, *J. chem. Phys.*, **89,** 63.
[25] TOMASELLI, M., 1990, *RF-Driven ^{13}C Spin Diffusion*, diploma thesis, ETH Zurich.
[26] SHAKA, A. J., KEELER, J., and FREEMAN, R., 1983, *J. magn. Reson.*, **53,** 313.
[27] MARICQ, M. M., 1990, *Adv. magn. Reson.*, **14,** 151.
[28] HAEBERLEN, U., 1976, *Advances in Magnetic Resonance, Suppl. 1. High Resolution NMR in Solids* (New York: Academic).
[29] CARAVATTI, P., BRAUNSCHWEILER, L., and ERNST, R. R., 1983, *Chem. Phys. Lett.*, **100,** 305.
[30] BURUM, D. P., LINDER, M., and ERNST, R. R., 1983, *J. magn. Reson.*, **43,** 494.
[31] CERNY, M., MALEK, J., CAPKA, M., and CHVALOVSKY, V., 1969, *Coll. Czech. Chem. Commun.*, **34,** 1025.
[32] FRÉCHET, J. M. J., DARLING, P., and FARRALL, M. J. J., 1981, *Org. Chem.*, **46,** 1728.
[33] SCHLOSSER, M., and SCHAUB, B., 1982, *Chimia*, **36,** 396.
[34] BECKER, H. G., *et al.*, 1984, *Organikum* (Berlin: VeB deutscher Verlag der Wissenschaft), p. 261.
[35] OVERBERGER, C. G., 1963, *Macromol. Synth.*, **1,** 4.
[36] SCHMID, M., 1988, Ph.D. Thesis, ETH-Zurich, Dissertation Number 8672.
[37] BURNS, R., JONES, D. T., and RICHTIE, P. D., 1935, *J. chem. Soc.*, 714.
[38] ATKINS, E. D. T., 1989, *Comprehensive Polymer Science* (Oxford: Pergamon), Vol. 1 p. 613.
[39] NATTA, G., CORRADINI, P., and BASSI, I. W., 1960, *Suppl. Nuovo Cimento*, **15,** 68.

[40] HESTER, R. K., ACKERMAN, J. L., NEFF, B. L., and WAUGH, J. S., Phys., 1976, *Phys. Rev. Lett.*, **36**, 1081; RYBACZEWSKI, E. F., NEFF, B. L., WAUGH, J. S., and SHERFINSKI, J. S., 1977, *J. chem. Phys.*, **67**, 1231.

[41] ROBYR, P., TOMASELLI, M., GROB-PISANO, C., MEIER, B. H., ERNST, R. R., and SUTER, U. W., 1995, (manuscript in preparation).

[42] RAPOLD, R. F., SUTER, U. W., and THEODOROU, D. N., 1994, *Macromol. Theory Simul.*, **3**, 19.

[43] MITCHELL, G. R., and WINDLE, A. H., 1984, *Polymer*, **25**, 906.

[44] SCHÄRPF, O., GABRYS, B., and PFEIFFER, D. G., Report of the Inst. Laue Langevin, No. 90SC26T Grenoble France.

[45] GABRYS, B., SCHÄRPF, O., and PFEIFFER, D. G., 1993, *J. Polym. Sci.* B, **31**, 1891.